

Upper mantle beneath Southeast Asia from *S* velocity tomography

Sergei Lebedev¹ and Guust Nolet

Department of Geosciences, Princeton University, Princeton, New Jersey, USA

Received 22 November 2000; revised 14 March 2002; accepted 21 March 2002; published 29 January 2003.

[1] We present a three-dimensional, *S* velocity model of the SE Asian-western Pacific upper mantle with 400-km lateral resolution. Using the novel Automated Multimode Inversion technique, we processed 4038 vertical-component seismograms and extracted 22,708 linear equations with uncorrelated uncertainties that constrain upper mantle structure. We used time-frequency windows to select signal with negligible proportion of scattered energy. The windows included the fundamental Rayleigh mode and *S* and multiple *S* waves. The observed range of *S* velocity variations is the widest (17–18%) in the upper 150 km of the mantle. High-velocity continental roots can reach beyond the present extent of the overlying Archean-Proterozoic crust by 500 km. Beneath some Precambrian units the roots are absent, which can be attributed to deformation and gradual destruction of the ancient lithosphere. At 120–150 km, *S* velocity beneath some cratons reaches 4.8 km/s; this can be accounted for by thermal and compositional effects. Beneath the Hainan Island area a low-velocity anomaly is observed from near the surface to the bottom of our model; the hot spot-type volcanism here may be caused by the deep-mantle Hainan plume. A low-velocity mantle domain underlies the south central Sea of Japan, surrounded on the surface by intraplate volcanoes. A deep-seismicity gap is present near 40°N in the Pacific slab subducting below and may result from a plume-slab interaction. A high-velocity anomaly is present in the transition zone beneath the northern boundary of the Yangtze Craton. We propose that the anomaly corresponds to subducted continental lithosphere, stagnant atop the 660-km discontinuity.

INDEX TERMS: 7218

Seismology: Lithosphere and upper mantle; 7260 Seismology: Theory and modeling; 7255 Seismology: Surface waves and free oscillations; 8180 Tectonophysics: Tomography; 8120 Tectonophysics: Dynamics of lithosphere and mantle—general; KEYWORDS: Hainan Plume, Yangtze Craton, Sino-Korean Craton, multimode surface waves, transition zone, continental lithosphere

Citation: Lebedev, S., and G. Nolet, Upper mantle beneath Southeast Asia from *S* velocity tomography, *J. Geophys. Res.*, 108(B1), 2048, doi:10.1029/2000JB000073, 2003.

1. Introduction

[2] The Southeast Asia-western Pacific (Figure 1) is a dynamic and tectonically diverse region with old and young subduction zones, abundant back-arc and intraplate volcanism, active seafloor spreading and, in continental Asia, ancient cratons and areas of extensive Cenozoic deformation. We present a three-dimensional (3-D) tomographic model of the upper mantle beneath the region that displays the expression of the tectonic phenomena and related deep processes in shear velocity anomalies. We describe in detail the characteristics and limits of applicability of the new tomographic constraints on mantle structure and point out the implications of our results for some of the outstanding problems of the SE Asian geology.

[3] The western Pacific is a distinct region on the surface (Figure 1), and a preview of our results shows that it stands

out in the upper mantle, as seen by shear waves (Figure 1, bottom). At an asthenospheric depth (170 km) it is “slower” (characterized by lower seismic velocities) than the surroundings. In the transition zone (470 km) it is mostly “faster” (higher velocities), due to the abundance of cold subducted material (one exception, a prominent slow anomaly, is beneath Hainan and the South China Sea).

[4] Continental SE Asia (as defined here) includes central and eastern China and Indochina and comprises three ancient continental blocks: North China, South China, and Indochina. The following summary of the tectonic history of the region is mostly after *Li* [1998].

1.1. Tectonic Background

[5] The North China Block, also known as the Sino-Korean Craton (Figure 2), consists of two major Archean (older than 2.5 Ga) continental nuclei surrounded by Paleoproterozoic (about 1.8 Ga) orogenic belts. One nucleus is approximately in the boundaries of the Ordos Basin (Ordos Plateau), and the other, larger one, is beneath and around the Bohai Gulf. Younger orogenic belts are located along the margins of the block. The South China Block includes two major Precambrian elements: the Yangtze Craton and the

¹Now at Department of Earth, Atmospheric and Planetary Sciences, Massachusetts Institute of Technology, Cambridge, Massachusetts, USA.

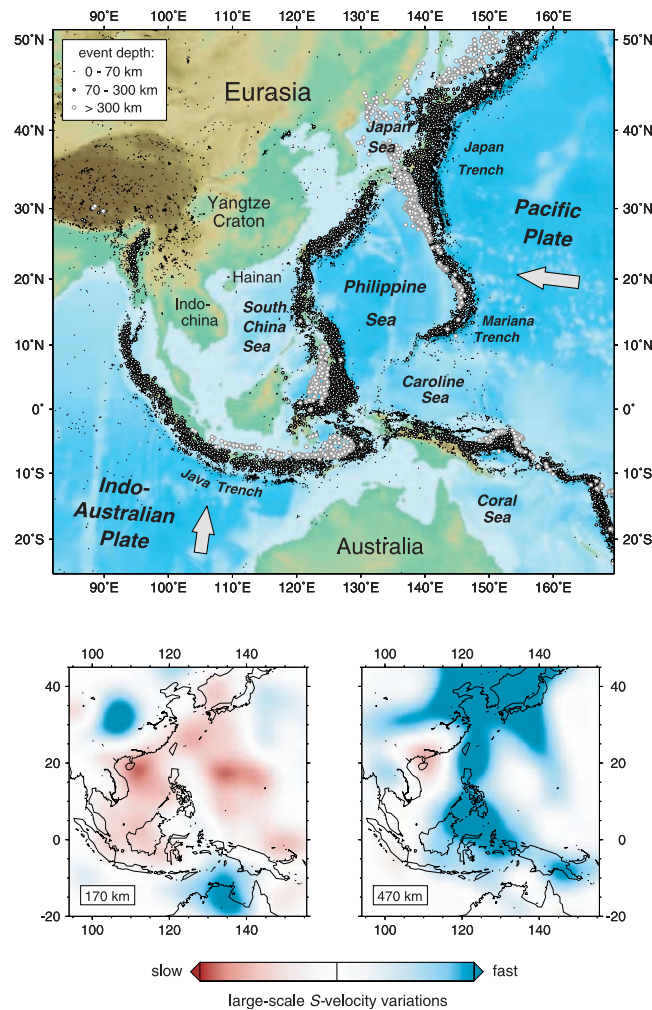


Figure 1. (top) Topographic map of the region. Seismicity is plotted using the hypocenters from the catalogue of *Engdahl et al.* [1998]. (bottom) Constant depth slices through a strongly smoothed tomographic solution. The limits of the color scale are ± 200 m/s (170-km slice) and ± 60 m/s (470 km).

Cathasia Block. The Archean nucleus of the Yangtze Craton is approximately within the boundaries of the Sichuan Basin; Paleoproterozoic basement is found in the vicinity of the basin and to the southwest; the rest of the basement is probably of the Grenville age (about 1.0 Ga). The Cathasia Block is situated along the coast (a part in the South China Foldbelt and a part underwater to the east) and is separated from the Yangtze Craton by orogenic belts of different ages, from about 1000 to 150 Ma. The Indochina Block also has a Precambrian core and probably extends to the northwest as the Shan Thai (Simao) Block [*Metcalfe*, 1996].

[6] The history of the North China and South China Blocks may be traced as far as 1.0 Ga, when both were a part of the supercontinent Rodinia; during the assembly of Rodinia, Cathasia first joined the Yangtze Block. Rifting within Rodinia started soon after 900 Ma; a rift formed but failed between Yangtze and Cathasia. The rift was mostly closed during the “Caledonian orogenic episode,” by 400 Ma. The closure completed later, in the Mesozoic. Active margins existed in the Paleozoic along both the south and north boundaries of the Sino-Korean Craton.

[7] The North China Block joined with the Mongolian terranes, presently situated to the north of the block, in the Permian (at 280–250 Ma), and around the same time, continental collisions began between the core of Eurasia, North China, and South China Blocks, the latter already joined with Indochina. The initial contact between the North and South China Blocks occurred at their eastern ends, probably resulting in the subduction of some of the Yangtze lower continental crust and lithosphere; the main phase of suturing followed at 240–170 Ma. Fold belts now found to the northwest of the Yangtze Craton were formed in Paleozoic-early Mesozoic. The suturing between North China-Mongolia and Siberia was complete around 150 Ma.

[8] As the relative motion between the continental blocks slowed down and finally stopped, a convergent margin developed along the southeast Asia coast. It caused widespread magmatism at 160–100 Ma and the development of a “basin and range province” along the coast (in the South China Foldbelt). At 115–100 Ma, the plate boundary may have been transform rather than convergent [*Osozawa*, 1998].

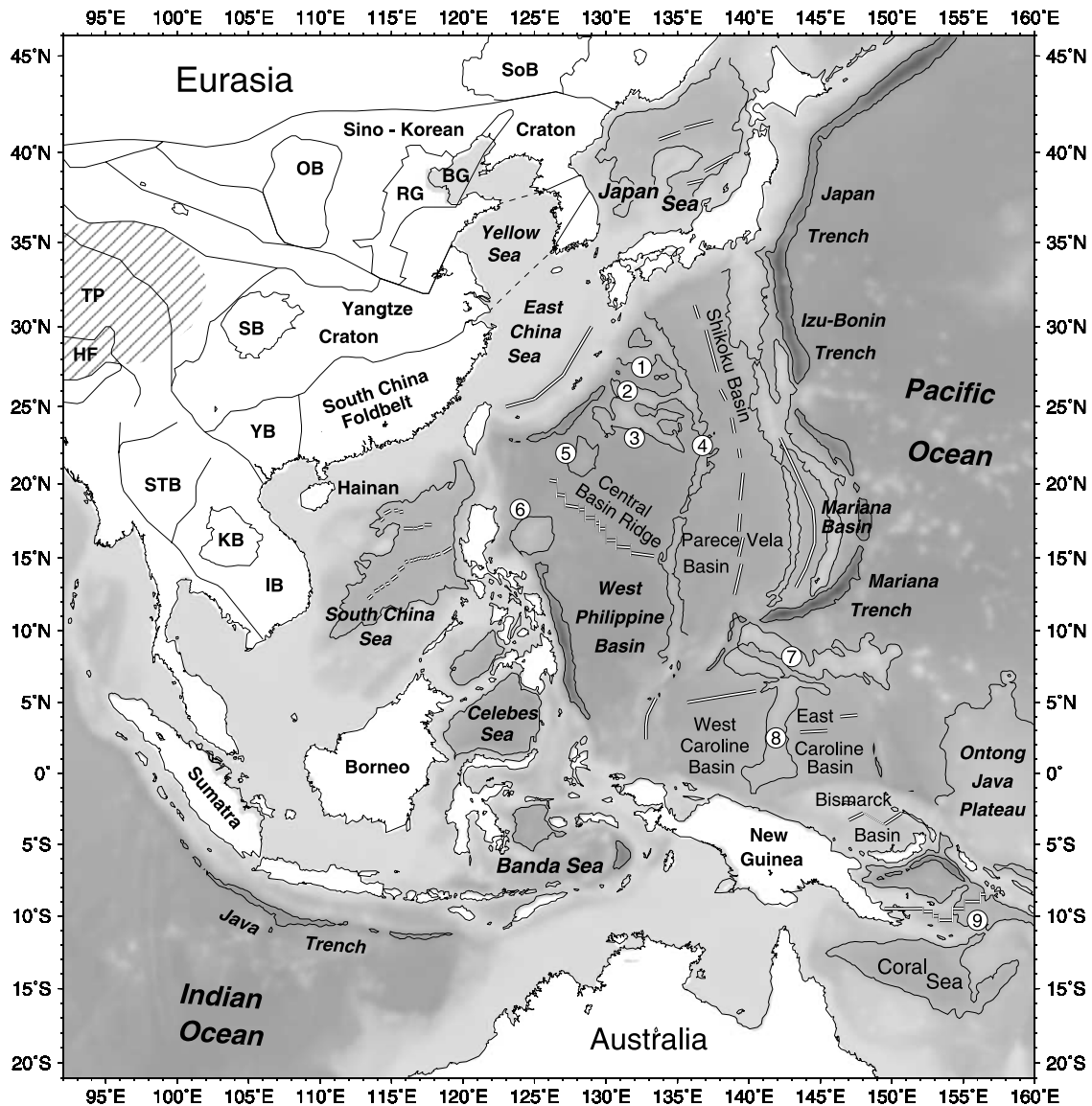


Figure 2. Tectonic sketch map of Southeast Asia and the western Pacific. Thick lines indicate the boundaries of major tectonic units, thin ones outline basins. Lighter (grey) lines show the boundaries of the blocks that are mostly outside the study region. The boundaries are after Zhang *et al.* [1984] and Packham [1996]. The hatched area is the Tibetan Plateau and surrounding mountain systems underlain by a crust thicker than 60 km, according to Zhang *et al.* [1984] and Li and Mooney [1998]. The abbreviations are BG, Bohai Gulf; HF, Himalaya fold system; IB, Indochina Block; KB, Khorat Basin (Khorat Plateau); OB, Ordos Basin (Ordos Plateau); RG, the eastern North China rift group; SB, Sichuan Basin; SoB, Songliao Basin; STB, Shan Thai Block; TP, Tibetan Plateau; YB, Youjiang Block. Selected marginal basins and underwater plateaus, ridges, and trenches are outlined with bathymetric contours, chosen for each feature. Double lines indicate spreading centers, active and extinct. Circled numbers identify 1, Amami Plateau; 2, Daito Ridge; 3, Oki-Daito Ridge; 4, Palau Kyushu Ridge; 5, Urganeta Plateau; 6, Benham Rise; 7, Caroline Ridge; 8, Eauripik Ridge; 9, Woodlark Basin.

[9] The India-Eurasia collision started at about 55 Ma and controlled the Cenozoic tectonic history of SE Asia. The collision caused the extrusion of the Indochina block south-eastward between 50 and 23 Ma and the opening of the South China Sea to accommodate it [Briais *et al.*, 1993]. Around 15 Ma the compressional regime and eastward motion of Indochina changed to extension and westward retreat. According to the escape tectonics scenario [Molnar

and Tapponnier, 1975], the subsequent eastward displacement of southern China and widespread rifting in the Sino-Korean Craton represent the next episode of the extrusion. Major north China's rift systems are located in the area of the Bohai Gulf on the east and along the perimeter of the Ordos Basin on the west, with more rifts in between.

[10] The Sea of Japan has opened at 30–15 Ma, probably in a pull-apart manner with simultaneous rotations of a

number of Japan's tectonic blocks [Jolivet *et al.*, 1995]; the opening mechanism of the sea is disputed.

[11] Almost all of today's seafloor in the back-arc basins of the western Pacific formed in Cenozoic. Back-arc basins have been opening and closing continuously; spreading centers and subduction zones formed and migrated following extremely complex patterns, influenced by collisions of continental and island arc crustal blocks [Hall, 1996]. The relatively old West Philippine Basin formed at about 60–35 Ma; its origin is debated [e.g., Seno and Maruyama, 1984]. The younger eastern half of the Philippine Sea plate was formed behind the Izu-Bonin and Mariana Trenches at 30–15 Ma [Mrozowski and Hayes, 1979; Chamot-Rooke *et al.*, 1987]; the East and West Caroline basins opened at 36–28 Ma [Weissel and Anderson, 1978]. Since 30–25 Ma, terrane accretion became more active in the southeast, where the Australian continent is now colliding with island arcs [Lee and Lawver, 1995].

[12] Deep mantle processes that accompanied the tectonic evolution are largely unknown. Perhaps, the most comprehensive record of the processes may be found in the seismic velocity structure of the mantle.

1.2. Seismic Imaging

[13] Seismic tomography has already led to important discoveries in the region. Arguably, the most significant results to date have been obtained in short-period, delay time studies. Van der Hilst *et al.* [1991] and Fukao *et al.* [1992] documented the complex morphology of the subducting Pacific lithospheric slab that appears to deflect in the transition zone (TZ) beneath the Japan and Izu-Bonin Trenches but descends into the lower mantle at a steep angle beneath the Mariana Trench. Recent regional and global delay time studies [e.g., Widiyantoro and Van der Hilst, 1997; Bijwaard *et al.*, 1998; Zhao *et al.*, 2000] provided more detailed images of the Pacific, Indo-Australian, and other subducting slabs in the region down to great depths in the lower mantle. Still, the resolution even in the upper mantle has been limited. Although the seismicity in the western Pacific is very high, it is uneven, and so is the distribution of seismic stations; this reduces the ray coverage and therefore the resolution of tomographic imaging using first *P* arrivals.

[14] Seismic structure of the regions with low seismicity and few stations can be constrained with surface waves. Southeast Asia was a part of the target area in many regional-scale projects. A number of fundamental mode studies concentrated on the Philippine Sea region [Seekins and Teng, 1977; Oda and Senna, 1994; Nakamura and Shibutani, 1998] and produced shear velocity values that generally correlated with seafloor age and surface features. Ritzwoller and Levshin [1998] and Curtis *et al.* [1998] used thousands of three-component seismograms and constructed group and phase velocity maps for the whole of Eurasia. Both sets of maps suggested that a high-velocity root underlies the Yangtze Craton, at contrast with the low velocities to the Southeast, beneath the coast of China and Indochina. For a comprehensive review of surface wave studies of Eurasia (with regional and global modeling), the reader is referred to Ritzwoller and Levshin [1998].

[15] During the last decade, efficient new techniques of multimode waveform inversion [e.g., Cara and Lévêque, 1987; Nolet, 1990; Gee and Jordan, 1992; Van Heijst and

Woodhouse, 1997; Debayle, 1999] extended the resolution of surface wave imaging down to the TZ. Multimode inversions include both the fundamental and higher modes of surface waves. Compared to the fundamental mode, higher modes sample greater depth intervals and therefore provide additional information on deeper structure. Constructive interference of higher modes produces arrivals of body waves, such as *S*, *sS*, or multiple *S*. Energetic arrivals of these waves are usually found on a seismogram either before the fundamental mode wave train or interfering with it. Strong interference often occurs at regional distances of a few thousand kilometers. In conventional fundamental mode measurements the interference amounts to contamination of the signal, and the seismogram or a part of its spectrum has to be discarded. Thus another advantage of a multimode technique is that it can utilize more measurements at shorter source-station distances, which allows to obtain information on averages over smaller volumes in the Earth and to include waves at higher frequencies, ultimately increasing the resolution of the imaging.

[16] Two recent regional multimode studies concentrated on the Philippine Sea region. Lebedev *et al.* [1997] used partitioned waveform inversion [Nolet, 1990; Van der Lee and Nolet, 1997b] and derived a 3-D shear velocity model for the Philippine Sea area constrained by about 280 seismograms. The study ascertained that ray theoretical inversions of multimode surface waves can produce useful resolution down to the TZ in a region as heterogeneous as the western Pacific. A puzzling low-velocity anomaly was detected beneath a long extinct spreading center, the Central Basin Ridge in the West Philippine Basin. Kato and Jordan [1999] combined regional surface and *S* wave data with *ScS* reverberation measurements and computed a path-averaged, radially anisotropic one-dimensional (1-D) *S* velocity model for the western Philippine Sea upper mantle. *ScS* reverberation measurements suggested that the lithosphere was unexpectedly thick, extending down to about 90 km depth. Both multimode studies involved labor intensive interactive processing of the seismograms, so that only a small portion of the available data could be processed and used.

[17] In this paper we introduce the novel Automated Multimode Inversion technique developed on the basis of the partitioned waveform inversion of Nolet [1990], show how its application results in a high-resolution, 3-D, *S* velocity model for the western Pacific and Southeast Asia, and present a geodynamic interpretation of the model. For the purposes of this introduction, we showed the slices in Figure 1 through a strongly smoothed version of the model. After the description of the tomographic procedure we shall present our preferred, high-resolution model.

2. Data and Inversion

[18] Our inversion procedure uses the two-step design by Nolet [1990]. After the initial selection of data we first inverted each seismogram in order to obtain a set of linear equations constraining the average *S* velocity structure between the source and the station. In contrast to the procedure outlined by Nolet [1990], a newly designed algorithm for time-frequency window selection was used to automate the waveform inversions [Lebedev, 2000]. In the second step, the linear system resulting from the first

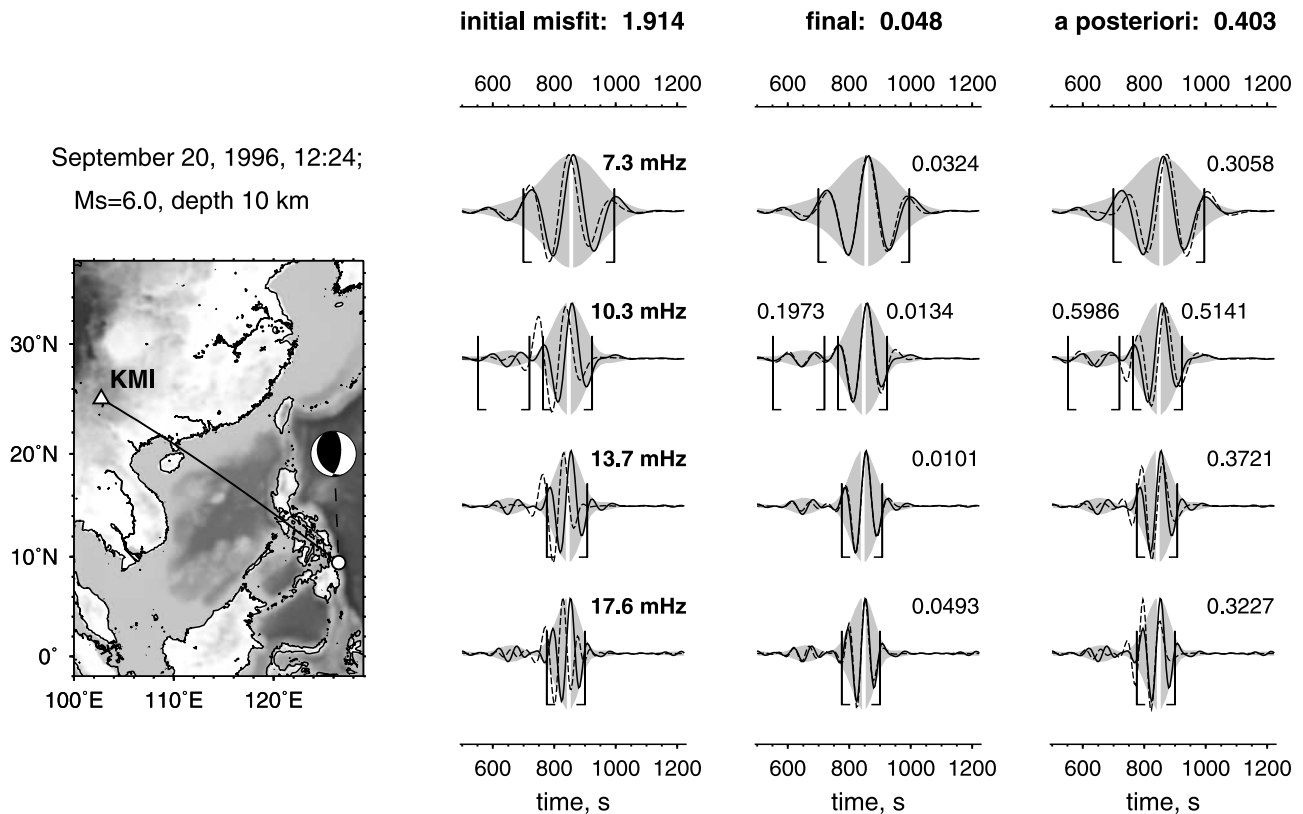


Figure 3. The waveform inversion procedure. (left) Locations of the event and the CDSN station KMI that produced the recording. (right) Waveform fits for a path-average 1-D model before the inversion (initial fit) and after the waveform inversion (final), and the fit predicted by the 3-D model (a posteriori). The traces are filtered using four closely spaced band-pass filters; the center frequencies of the filters are specified next to the waveforms in the first column. The recorded signal is drawn with a solid line, and the synthetics are drawn with a dashed line. Envelopes of the data traces are shaded grey; the maxima of the fundamental mode envelopes are marked with white vertical lines. Half brackets denote the time windows selected for each filtered waveform. The values of the misfit in each window are shown next to the windows in the two columns on the right.

step was solved for a 3-D, S velocity model, as described by *Van der Lee and Nolet* [1997b].

2.1. Waveform Inversions

[19] Our new Automated Multimode Inversion (AMI) is well equipped for processing the data from the western Pacific, a region of very high seismicity and high heterogeneity at a broad range of scales. Efficient selection of the wave trains uncontaminated by scattered waves ensured accuracy of our measurements. Full automation allowed us to take advantage of the enormous volume of available data and use a large waveform data set to constrain the 3-D tomographic model.

[20] A basic assumption behind the inversion scheme is the validity of the surface wave ray theory (WKB approximation), which does not account for scattering. Theoretical considerations and numerical modeling [e.g., *Kennett and Nolet*, 1990; *Wang and Dahlen*, 1995] show that scattering causes phase shifts that translate into measurement errors. Because of high heterogeneity in the upper mantle, the amount of scattered energy on the seismograms recorded in the region is relatively large. The proportion of scattered energy and its distribution in the time and frequency domains is different for every seismogram, depending on

the locations of the source and receiver and the frequency-dependent radiation patterns of the modes [*Meier et al.*, 1997; *Lebedev and Nolet*, 1998]. Many seismograms cannot be modeled and inverted using the surface wave ray theory. For others, only parts of the signal and only in selected frequency bands can be used.

[21] Our approach in identifying the usable parts of the signal is based on the assumption inherent in many waveform analysis schemes: the measurement is considered reliable if the data-synthetic misfit is small. This intuitively reasonable assumption is supported by theoretical studies [*Wang and Dahlen*, 1995; *Furumura et al.*, 1999; *Meier and Malischewsky*, 2000] that suggest that scattering affects both the phase and the shape of the wave train. A wave group interfering with scattered waves is distorted and less likely to be matched by a WKB synthetic.

[22] Figure 3 illustrates the implementation of the AMI procedure. Waveforms in five time-frequency windows are inverted simultaneously in order to constrain the average S velocity structure along the source-station path across the South China Sea. The first column of waveforms shows the misfit before the inversion. Synthetic seismograms for an initial (background) path-average 1-D model are computed by the summation of the first 30 Rayleigh modes. Following

Nolet [1990], we use nonlinear optimization to find the perturbations to the initial model that minimize the data-synthetic misfit (“final” in the middle column). In this study we varied only S velocity and crustal thickness, with P velocity, density, and the quality factor kept unperturbed. The perturbations are expressed in the form of linear equations with uncorrelated uncertainties that constrain the structure along the path and are the ultimate result of the waveform inversion.

[23] We developed a set of strict criteria for the selection of time-frequency windows in which the proportion of scattered energy is small. We require the waveform fit to be almost exact: the misfit (net relative data-synthetic difference of squared amplitudes) has to be less than 5% for the fundamental mode and less than 20% for the higher-mode part of the seismogram. In the example, four fundamental mode time windows and one window with an S wave display sufficiently good fit and are accepted. All our fundamental mode fits are of the same quality or better than that at the bottom of the middle column (4.9% at 17.6 mHz) and the higher-mode fits are similar or better than that of the S wave (19.7% in the window on the left at 10.3 mHz) in the example. The fit of the fundamental mode has to be acceptable in at least three partially overlapping, relatively narrow frequency bands, for a total frequency band at least one octave wide. All the accepted fundamental mode frequency windows have to be defined by consecutive closely spaced filters, with no skips allowed.

[24] We select only complete wave trains: the amplitude of the envelope of the signal at a time window boundary has to be at least 4–5 times smaller than that of the nearest envelope maximum inside the window. This ensures that the phase of the wave train in the window is not significantly affected by the interference with the waves outside. Initially, a single time window containing the whole waveform is attempted at each frequency. At 10.3 mHz in the example (Figure 3), the wave trains of the fundamental mode and the S wave can be separated into two different time windows. Because the fit in the gap between these windows is poor, the gap is excluded and the two separate windows are applied. At higher frequencies in the example (13.7 and 17.6 mHz), the fit is acceptable only for the fundamental mode.

[25] The energy of the synthetics is equalized with that of the data in each window. This adjustment isolates the shape of the wave train from its absolute amplitude. The latter is proportional to the scalar moment of the event, which is a relatively uncertain parameter in moment tensor catalogues (Helffrich [1997] estimated the error at ± 40 –60%). Once the absolute amplitude is removed, the waveform depends on the phase of the modes and their relative amplitudes in the time window. A big practical advantage of the energy equalization is that the misfit value becomes a convenient measure of the quality of the waveform fit. It is now possible to select acceptable windows by comparing the misfit with a chosen threshold of a few percent (this would not work with an amplitude uncertainty of a few tens percent).

[26] In Figure 4, the data and the initial and final synthetics of Figure 3 are filtered using a single, wide frequency band that covers all the four bands of Figure 3. A comparison of Figures 3 and 4 points to the advantages of the multiple time-frequency windows. First, the contributions to the misfit function of the signal at all frequencies can

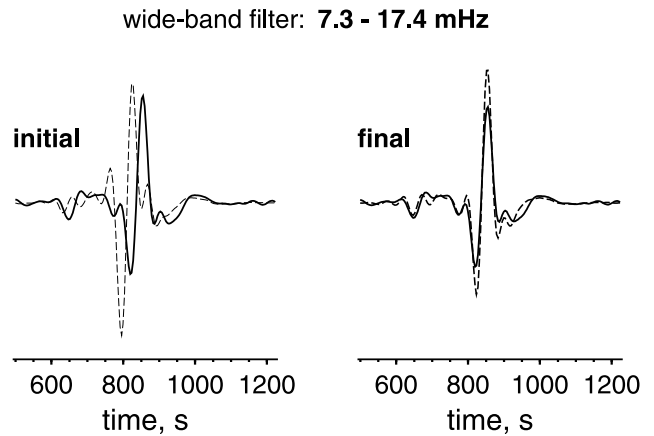


Figure 4. The waveform fits from Figure 3 filtered using a single, wide frequency band (7.3–17.4 mHz). The actual seismogram is shown with solid lines, the synthetics with dashed lines. The “final” synthetic is computed using the best fitting 1-D average model obtained in the multiple-window waveform inversion of Figure 3. The energy of the data and synthetic is not equalized.

be set to equal (or weighted if desired), regardless of what the dominant frequency of the radiation at the source was. Second, if acceptable signal at one frequency overlaps in time with scattered waves at another frequency, the multiple time-frequency windows enable us to extract information from the former while avoiding the latter. Finally, the waveforms in narrow frequency bands are much simpler than in wide ones. Most our fits have one or more simple wave trains in each window and look very similar to the example in Figure 3. This simplicity allows us to aim at low misfits and is essential for the misfit value criteria to be an efficient data selection tool. In this first large-scale application of the new PWI implementation (AMI), we use very strict selection criteria and low misfit thresholds. These values can be easily adjusted in future applications, according to characteristics of data sets or objectives of studies.

[27] The starting (background) model for the waveform inversion should preferably be similar to the actual path average and, at the same time, contain minimal a priori complexity. We used two sets of background models (Figure 5): oceanic (slower) and continental (faster). Mantle velocities were the same in different models of each subset, but the crustal thickness and the depth to the seafloor varied, the end-members being an oceanic model with a 5 km water layer and a 6-km crust and a continental model with a 75 km crust (for the paths across Tibet). The average depth to the Mohorovičić discontinuity (Moho) along the path was one of the inversion parameters, as described by Das and Nolet [1995]. To keep perturbations small, AMI iterated over background models with different Moho depths until the one with the smallest required crustal thickness perturbation was found.

[28] Anelastic dispersion was computed according to assumed attenuation models that showed agreement with the data (Figure 5). In order to minimize the uncertainties due to unknown lateral variations in attenuation structure [Liu *et al.*, 1976], all the waveform inversions were performed for S velocity at a reference period of 50 s (close to

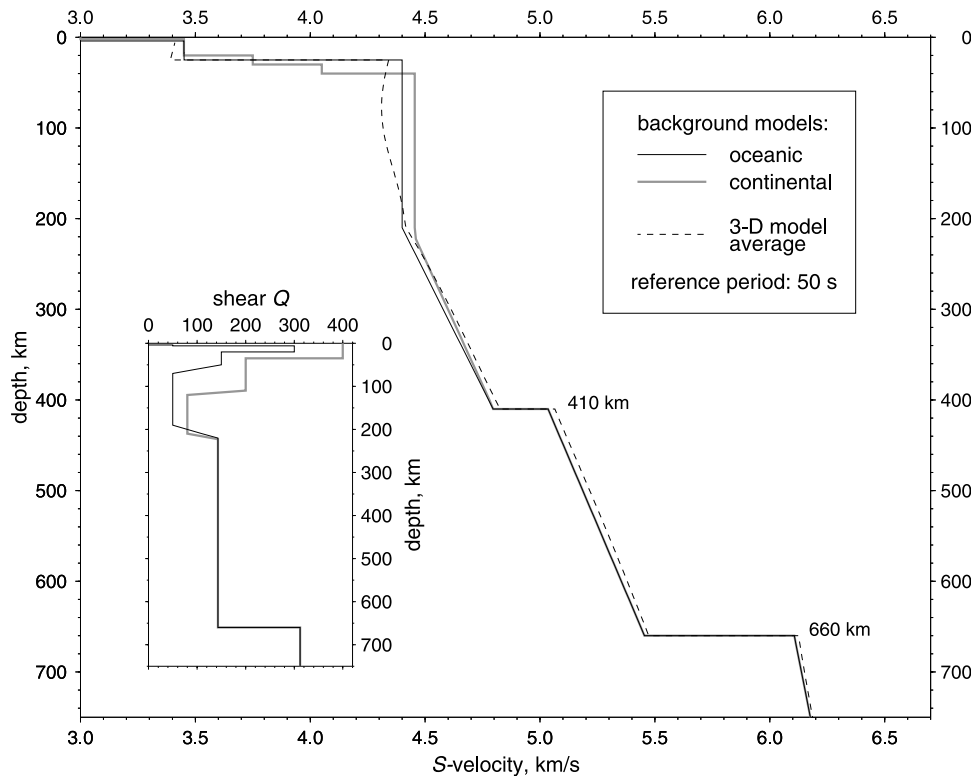


Figure 5. Examples of oceanic and continental background models used in the waveform inversions. The oceanic model with a 25-km-deep Moho (solid black line) is also the starting and reference model of the 3-D inversion; the S velocity anomalies in the 3-D model are relative to this model. The 1-D average of the 3-D model is drawn with a dashed line. Insert shows the attenuation models used in the waveform inversions.

the middle of a typical frequency band). The 3-D model computed in the subsequent linear inversion contains S velocities at the same reference period, 50 s.

2.2. Data Selection

[29] We started with all the events that occurred from 1994 to 1998 in or near the western Pacific for which the Harvard centroid moment tensor (CMT) solutions which we use here were available [e.g., *Dziewonski et al.*, 1994]. About 20,000 vertical-component, long-period recordings of the events at the stations of the Global Seismographic Network (GSN), the Chinese Digital Seismic Network (CDSN), and the Digitized World-Wide Standardized Seismograph Network (DWWSSN) in the region were retrieved from IRIS-DMC. We did not process earlier data because the accuracy of the moment tensor solutions and event locations is likely to decrease for older events, mostly due to a smaller number of stations available at the time. If we included data too old, the positive effect of the marginal improvements in the azimuthal path coverage would be offset due to larger systematic errors in the data set (strictly speaking a result of modeling, earthquake locations and mechanisms from published catalogues enter our inversions as a type of data). The particular starting date (1 January 1994) was chosen because since then the Harvard moment tensors were computed using an improved attenuation model [*Dziewonski et al.*, 1994]. Locations and origin times of the events were taken from the catalogue of *Engdahl et al.* [1998].

[30] The number of seismograms was reduced to about 12,000 after we set aside the near-nodal data and ran

automated quality checks to detect clipped and defective records. Still, many of the remaining records were contaminated by scattering (both near the source [*Van der Lee*, 1998] and elsewhere in the source-station region) and noise. AMI extracted useful signal from 4038 seismograms of the final data set (Figure 6), rejecting the rest. The processing resulted in a set of 22,708 linear equations constraining S velocities and Moho depths beneath the region. The depth of the earthquakes in the final data set is up to about 500 km; the moment magnitude ranges from 4.9 to 7. The source-station path length ranges from about 8° to 80° , with median and average around 30° .

[31] The fundamental mode was inverted for all the paths, with optimal frequency bands and time windows selected in each case (if the fundamental mode waveform fits did not pass selection criteria, the seismogram was discarded). Periods up to 350 s were included for some of the longer paths, periods down to 13 s for some of the shorter ones. Higher bound of the frequency windows was usually where scattering became unacceptably strong. For longer paths, only lower frequencies could be used (e.g., at distances longer than 7000 km, no signal was selected at periods below 45–50 s). Periods smaller than 4 times the event duration time were always excluded.

[32] Distinct higher-mode wave groups remained on 1721 processed seismograms. On many others, no clear multiple- S arrivals are visible, but the higher modes are included in the early part of the fundamental mode wave train, so that waveform fitting still extracts information from higher modes.

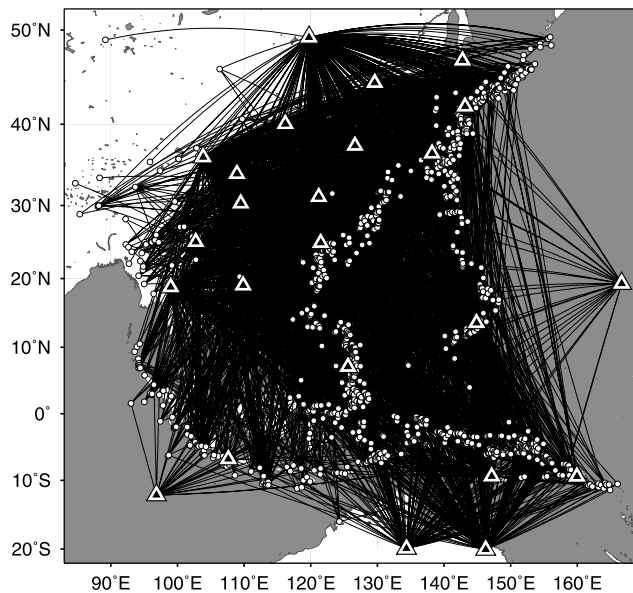


Figure 6. Ray path coverage achieved with the 4038 seismograms of our data set. Circles and triangles show the locations of the events and stations, respectively.

[33] Most of the higher-mode information came from the waveforms of the S , SS , and SSS waves, often triplicated and interfering with each other. We did not expect to sample the lower mantle beneath the region sufficiently to retrieve its structure and used only the S and multiple S waves that penetrated no deeper than about 800 km (epicentral distances less than 35° for S and 70° for SS waves). Another reason to avoid deep-diving S waves was that here we computed synthetics using simple mode summation, ignoring the three-dimensional structure of the body wave sensitivity volumes [Marquering *et al.*, 1998]. At shorter distances, the sensitivity zones are represented reasonably well by the 1-D basis functions of the path-average modeling, especially for the multiple S waves.

2.3. Three-Dimensional Inversion

[34] The 3-D model was obtained in an LSQR inversion with damping and horizontal smoothing. The procedure is described by Van der Lee and Nolet [1997b], and here we only discuss the details particular to this study.

[35] The 1-D reference model for the linear inversion (modified from PEM [Dziewonski *et al.*, 1975]) has a 3-km water layer and a 22-km-thick crust with a 2-km sediment layer (solid black line in Figure 5). It is close to the 1-D average of the resulting 3-D model (dashed line) but has a constant 4.4 km/s S velocity layer between 25 and 210 km depths. The advantage of such a simplified background model is that no a priori assumptions on the velocity variations with depth are imposed on the solution. The LSQR inversion starting with this reference 1-D model resulted in a 71% variance reduction. The solution of the inverse problem contains a 3-D S velocity model and a map of depths to the Moho.

[36] Our Cartesian grid had a knot spacing of 75 and 67 km in the horizontal and vertical directions, respectively. Trilinear interpolation was used to build the system of linear equations and to determine the value of the solution at a

given point. The damping was uniform and penalized the Euclidean norm of the solution at every knot of the grid. The damping parameter was 1.0; the dimensionless system of the 22,708 equations was normalized with a priori uncertainties of 220 m/s for S velocities and 10 km for Moho depths.

[37] The uniformity of both the grid and the damping ensures that the solution is not biased because of irregularities of parameterization [Van der Lee and Nolet, 1997b] but has two other important effects on the solution. First, it imposes limits on the vertical resolution in the crust and uppermost mantle. To keep the size of the problem manageable, we had to adopt a vertical knot spacing of 67 km. This effectively averaged out the small-scale vertical heterogeneity in the upper few tens of kilometers that could otherwise be reconstructed from higher-frequency fundamental mode measurements. Second, the solution in the parts of the model with relatively weak data sampling is overdamped. The overdamping affects not only poorly covered parts of the model, but also those with intermediate sampling. The linear equations that we extracted from our waveforms contain more information on the upper 200 km of the mantle than on deeper layers. The damping parameter was chosen so as to retrieve correctly the amplitude of the best sampled anomalies. Although the data sampling in the deeper upper mantle is still adequate, the magnitudes of anomalies there are underestimated by the model, especially in the lower TZ. Such magnitude bias is common in damped tomographic inversions; the solution for the problem may be in grid optimization algorithms, currently being developed [e.g., Nolet *et al.*, 1999; Montelli *et al.*, 2000].

[38] Smoothing in our inversion served two purposes: to imitate the wide sensitivity volumes of long-period waves and to suppress the artificial rough structure in the model caused by errors in the data. Perturbations along each source-station path were smoothed horizontally in the directions perpendicular to the path, the value of the smoothing function linearly decreasing from the maximum on the path to zero at a chosen distance (the half width of the smoothing function). The effect of smoothing is apparent as we compare the model obtained with a 660-km smoothing half width (Figure 1) and our preferred model, smoothed over 400 km (sections 3 and 5).

[39] The solution for Moho depths is shown in Figure 7, along with a topographic map and the $5^\circ \times 5^\circ$ map of Mooney *et al.* [1998] for comparison. The Moho map appears to be fairly accurate, an indication that the effect of crustal modeling errors on the mantle shear velocity model is small.

[40] The “a posteriori” synthetics computed using the averages through the 3-D model along the source-station paths [Van der Lee and Nolet, 1997b] are reasonably close to the data (Figure 3, right column), although not as close as the ones obtained in the waveform inversion. Relatively large errors in source locations and mechanisms are to be expected in the heterogeneous western Pacific, and the a posteriori misfits show how the errors averaged out.

3. Resolution Tests

[41] The accuracy of the imaging depends on the data coverage and errors in the data and approximations. The effect of the path coverage can be examined using resolution

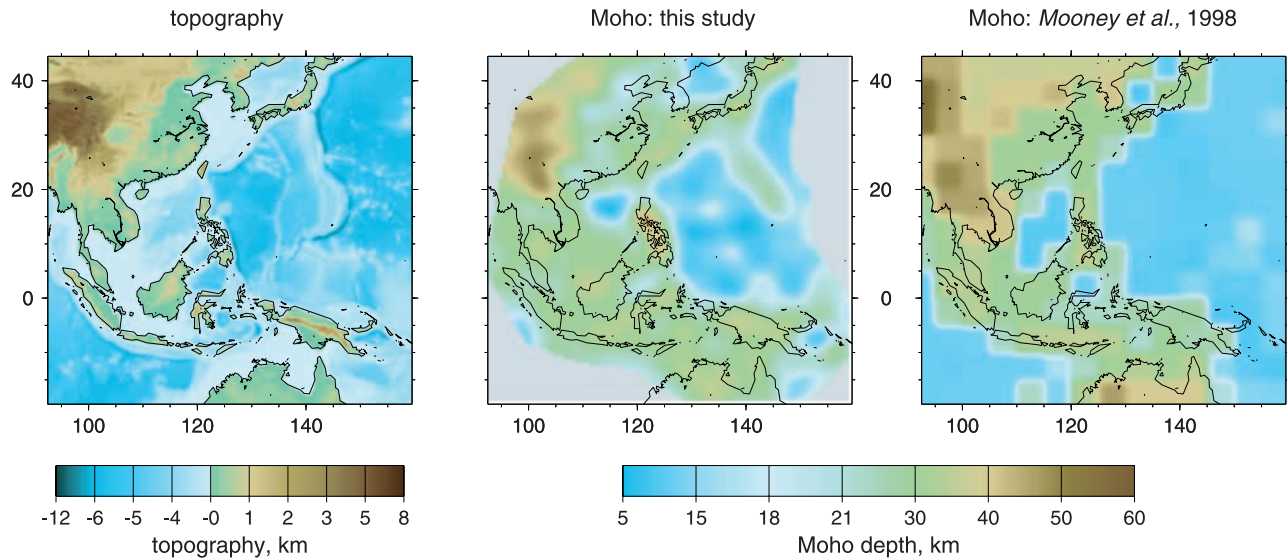


Figure 7. (left) Topographic map of the region. (middle) Estimated map of Moho depths obtained in our inversion. (right) Depths to the Moho according to the $5^\circ \times 5^\circ$ map of *Mooney et al.* [1998].

tests (Figure 8). In the upper 150 km of the mantle, we are able to retrieve both the shape and magnitude of the anomalies of the checkerboard patterns. Perturbations in the upper 150–200 km are constrained primarily by the fundamental Rayleigh mode. At 300 km, its resolving power weakens and is complemented by that of the higher modes; in the TZ resolution is provided by higher modes only. At these depths, the magnitude of the anomalies is underestimated.

[42] When the actual model (Figure 9) was used as an input pattern, the locations and shapes of the anomalies were retrieved almost exactly (94% variance reduction); the magnitudes of deeper anomalies decreased because of damping, especially in the lower TZ (by a factor of 1.5–3). In a series of tests, the actual model in the upper 150, 200, or 300 km was used as an input pattern; perturbations were zero everywhere below. In the output, the strongest shallow anomalies were smeared down by 50–100 km, but no significant deep artifacts appeared. We also computed separate models of the continental SE Asia and the oceanic part of the region, using sources and stations in those areas only. The result was a general decrease in resolution due to sparser path coverage, particularly near the boundary between the two subregions. Away from the boundary, however, both models were in agreement with the one constrained by the complete data set.

[43] Because the resolution tests do not account for errors in the data and assume the validity of adopted approximations, resolution estimates from the tests can be optimistic. The largest errors in our data are probably in event locations, followed by those in CMT solutions. Although random mislocations are unlikely to be important, given the large volume of the data we use, there is evidence that events in the western Pacific may be located with significant systematic errors [*Lebedev et al.*, 1997; *Bijwaard et al.*, 1998].

[44] A likeness of a “ground truth” test for the model is offered by the subduction-related seismicity, which reveals the locations of the fast-to-slow transitions across deep-sea trenches in the upper 100 km of the mantle (from fast

oceanic lithosphere to slow asthenosphere beneath the volcanic arc) and the high-velocity subducting slabs. In Figure 9 we superimpose seismicity [*Engdahl et al.*, 1998] on cross sections through the model. As expected, the lines of seismicity at 60 and 100 km coincide with sharp velocity contrasts (located with a precision of 100–400 km, depending on the local ray path coverage). Active spreading centers in the Mariana (12° – 22° N, 143° – 144° E) and Bismarck (4° S, 147° – 153° E) Basins are particularly slow, with shear velocities down to about 4 km/s at 100 km depth. Below 200 km, a pattern of high-velocity subducting slabs dominates the oceanic part of the region. We estimate the lateral resolution of the imaging at 400 km, equal to the a priori chosen smoothing length. On a constant depth slice we expect to see a 50–100 km thick slab as 500 km wide. The high-velocity anomalies around the Philippine Sea are indeed about this thick (Figure 9, 250 km), with deep earthquakes located within the slab images, which suggests that the lateral resolution of around 400 km is achieved.

[45] According to seismicity, plate tectonic reconstructions, and *P* delay tomography [e.g., *Hall*, 1996; *Widiyantoro and Van der Hilst*, 1997; *Lallemand et al.*, 1998], a few closely spaced slabs are subducting beneath the Banda and Molucca Seas (8° S– 5° N, 124° – 128° E). The corresponding high-velocity anomalies are less than 400 km apart, and their images in our model are averaged into a single one, near 3° N, 124° E. The Banda subduction zone (around 6° S, 127° E) forms a half circle that is about 500 km wide at shallower depths; the arc shape is resolved at 150–200 km depths (see the cross sections in section 5).

[46] The good correspondence between the patterns of seismicity and the retrieved *S* velocity variations suggests that errors in the data and approximations are unlikely to have caused significant artifacts. The model offers relatively uniform 400-km resolution beneath the SE Asia and western Pacific. In parts of the region, short-period, delay time studies resolved finer detail, in particular near subducting lithospheric slabs. Our model is in agreement with these

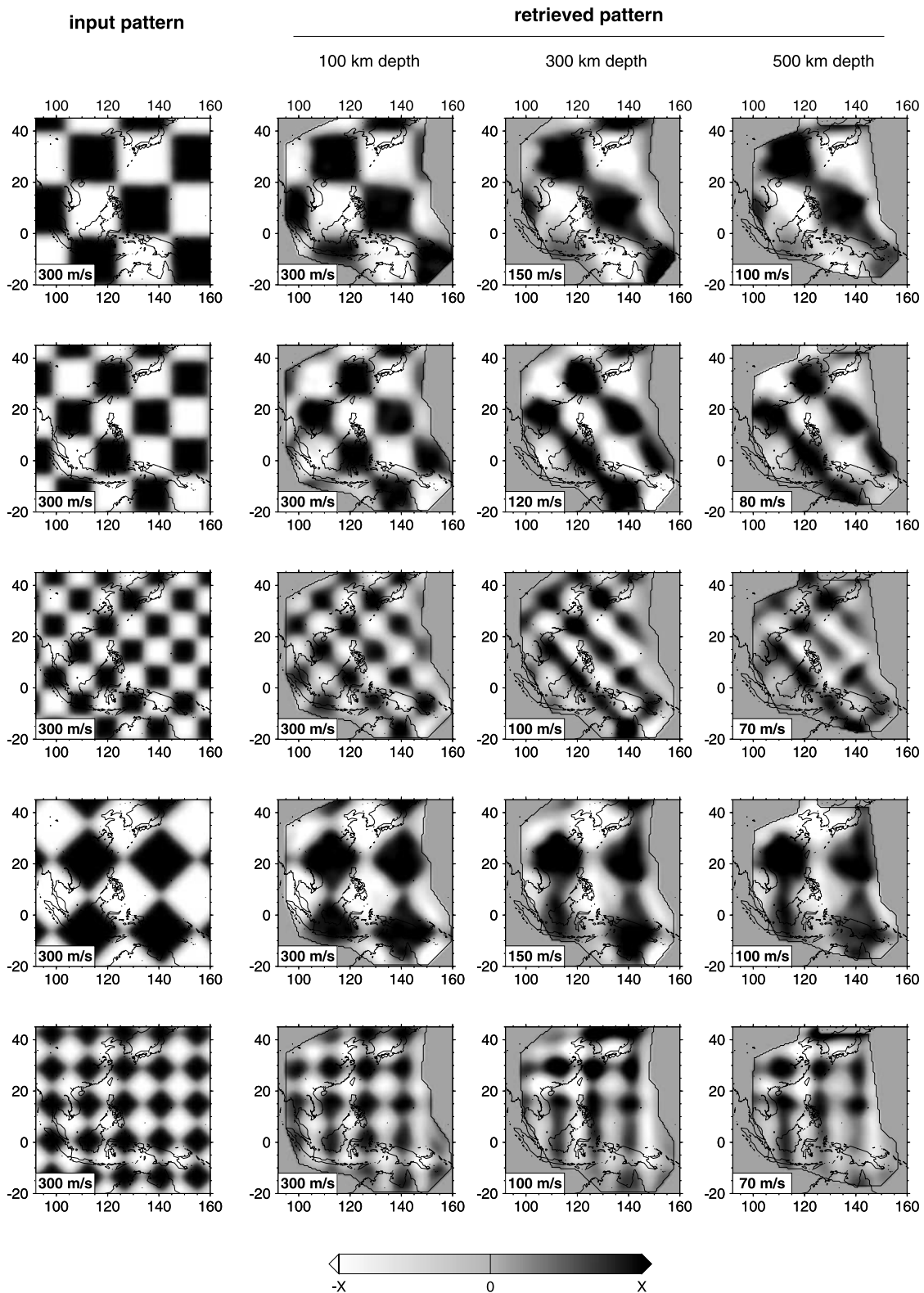


Figure 8. Fifteen checkerboard resolution tests. The inversions were regularized exactly as the inversion of the real data. The column on the left shows the input patterns, each used for three tests at different depths; the output of the 100-, 300-, and 500-km depth tests is shown to the right. In the input, the ± 300 m/s synthetic anomalies extend across a 200-km depth interval containing the depth indicated. The square sizes in the five rows of plots are, top to bottom, $20^\circ \times 20^\circ$, $15^\circ \times 15^\circ$, $10^\circ \times 10^\circ$, $20^\circ \times 20^\circ$, and $10^\circ \times 10^\circ$. The limits of the grey scale X are different for different plots and are given in the lower left corners of the frames. The retrieved patterns are shown only in the well-sampled part of the region, slightly shrinking with depth. The actual model will be plotted in the same well-sampled part.

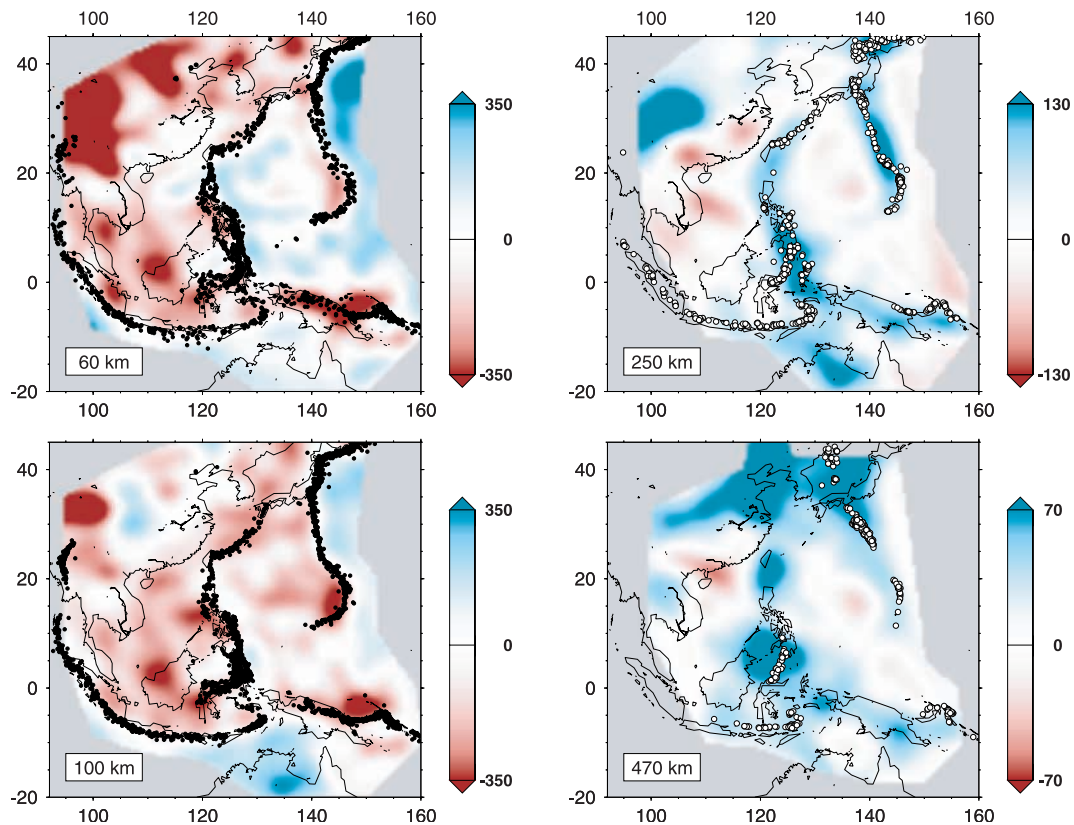


Figure 9. Constant depth cross sections through the model with earthquake hypocenters from *Engdahl et al.* [1998] superimposed as solid circles in the upper 100 km and as open circles at greater depths. S velocity variations (m/s) are relative to the reference model in Figure 5.

results, which gives us confidence in the features in the rest of the region, some of them never imaged before.

4. Interpreting the Tomographic Constraints

[47] Our new constraints on the structure and dynamics of the SE Asian upper mantle are the anomalies in the tomographic model, in particular their locations, shapes and magnitudes. The S velocity model complements the results of high-resolution P delay studies in two ways. First, the surface waves and regional S and multiple S waves that constrain the model sample the whole region, not only the areas with high density of sources or stations (such as subduction zones). Second, the sensitivity of S velocities (β) to the conditions in the mantle differs from that of P velocities (α). Low temperatures are likely to cause similar (primarily “anharmonic” [Karato, 1993]) relative increase in α and β , with $R = \delta \ln \beta / \delta \ln \alpha$ estimated at 1.1 to 1.4 in the upper 200 km of the mantle [Sobolev et al., 1996; Goes et al., 2000]. The conditions that decrease the velocities, including high temperatures and the presence of partial melt or volatiles, have a much larger effect on β than on α , with R exceeding 2 [Goes et al., 2000]. The locations where such conditions occur are thus easier to detect using S wave field observations.

4.1. Resolution

[48] The value of the resolution length equals the minimum distance between two anomalies of the same sign in

the Earth at which they can be distinguished on the tomographic image (Figures 10a and 10b). Equivalently, this length is the half width of the image of a hypothetical δ function perturbation in the Earth (Figure 10a). The resolution itself is inversely proportional to the resolution length, hence higher resolution is associated with a shorter resolution length, or finer detail resolvable in the Earth. Our model is characterized by a 400-km lateral resolution. An actual small-scale isolated feature would appear 400 km wide on our images, and a 100-km-wide anomaly in the real Earth would appear about 500 km wide. Closely spaced (<400 km) anomalies of the same sign will merge into a single one (Figure 10b). The wider image of a narrow anomalous region in the Earth would also underestimate the magnitude of the anomaly. In other words, the S velocity values in the model represent averages over 400 km (Figures 10b and 10c).

[49] Locations of fast-to-slow transitions can be determined with an uncertainty that is smaller than the resolution length (Figure 10d). However, an anomaly of small lateral extent may be overshadowed by a larger neighboring feature (Figure 10e). The vertical resolution length of our tomography is from 70 km in the upper to about 150 km in the lower part of the model.

4.2. Interpretation

[50] Tomographic images alone, especially one-wave-type (β or α) images, do not offer explanations for the

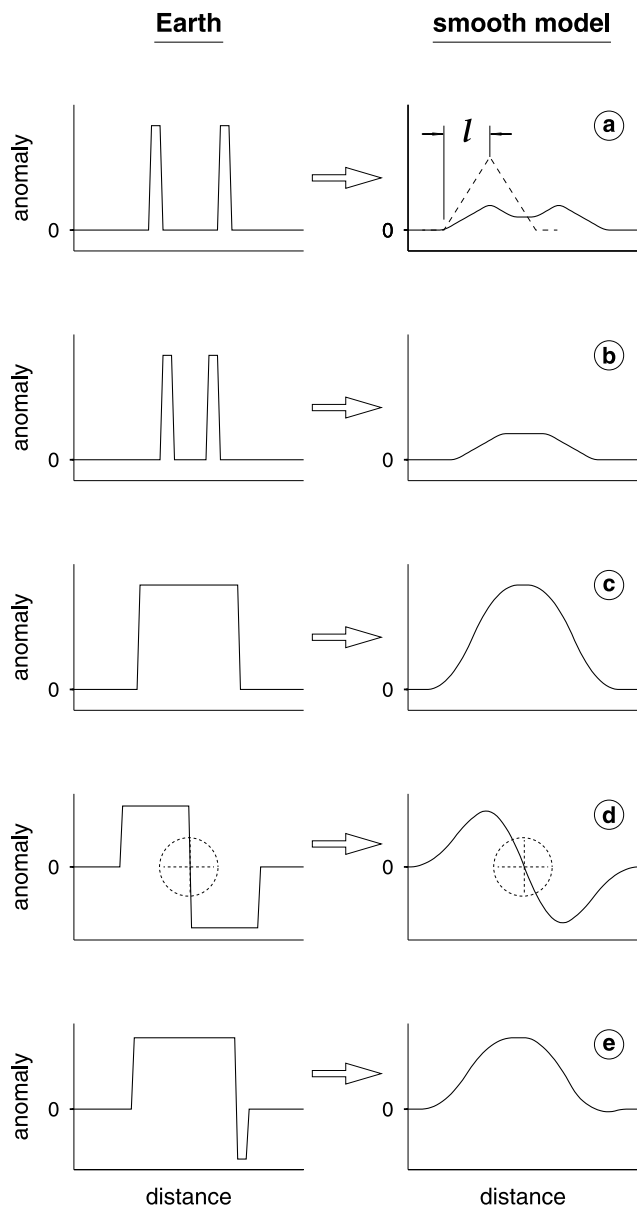


Figure 10. Schematic depiction of the effects of averaging on finite resolution tomographic images. (left) Hypothetical “true” anomalies in the Earth; (right) expected images of the anomalies. The value of the “imaged” anomaly at a point is an average over the values around the point, weighed by the smoothing function shown with a dashed line in Figure 10a, right. The half width of this function is the resolution length l . (a) Two narrow anomalies at a distance longer than l can be distinguished on the image; (b) anomalies at a distance shorter than l cannot be distinguished; (c) the magnitude is mapped accurately for anomalies of sufficient width, at least twice l ; (d) fast-to-slow transitions can be retrieved with good accuracy; the crosses drawn with dashed lines indicate zero crossings and are in the same location on both plots, left and right; and (e) a narrow anomaly disappears in the shadow of a wider neighboring one.

origin of seismic velocity anomalies. Both positive and negative anomalies can have a number of causes.

[51] First, S velocity in the rock at a given depth will vary with temperature. High (low) velocity is indicative of an anomalously low (high) temperature. Because of seismic attenuation, a high-temperature anomaly is expected to cause a larger relative change in seismic velocities than a low-temperature one of the same magnitude [Karato, 1993].

[52] Partial melting, whether or not due to relatively high temperatures, may cause a large decrease in β . The magnitude of the reduction will depend on the melt fraction and very strongly on the pattern of melt distribution between the solid grains of the rock [Walsh, 1969; Schmeling, 1985].

[53] An injection of small amounts of volatiles, such as water, can decrease shear velocity dramatically, both directly and through the decrease of the solidus temperature; the low velocities at 100–200 km depths landward of subducting slabs are attributed to the dehydration of subducted oceanic crust [e.g., Iwamori, 1998]. Compositional (chemical) heterogeneity in the mantle generally translates into seismic velocity heterogeneity [e.g., Nolet and Zielhuis, 1994; Sobolev et al., 1996; Griffin et al., 1998a; Goes et al., 2000].

[54] Finally, seismic velocity anomalies may be due to seismic anisotropy. The main cause of upper mantle anisotropy is thought to be the preferential alignment of olivine crystals in response to shear strain in the mantle [Savage, 1999]. Here we inverted for the isotropic speed of the vertically polarized S wave (SV), assuming that the dense coverage with crisscrossing paths averages out the azimuthal variations at each point in the model. Errors due to this assumption are probably small in the well-sampled part of the model that we plot (Figures 8 and 9) and discuss. Simons et al. [2002] used PWI to constrain azimuthally anisotropic structure of the Australian upper mantle and detected anisotropy of up to 4%. However, isotropic SV variations in the parts of Australia with dense ray path coverage depended little (<1%) on whether or not anisotropy was allowed by the parameterization. This result suggests that in the well-sampled (plotted) part of the model presented here the trade-offs between the isotropic and anisotropic structure are unlikely to produce errors exceeding 1%.

5. Overview of the Tomographic Constraints

[55] Figures 11 and 12 show the distribution of S velocity anomalies at eight depths in the upper mantle. On average, the velocities are low in the upper 200 km and relatively high below (see also the 3-D model average profile in Figure 5). Our reference model is close to the average profile; in the upper 200 km it is also not far from PREM [Dziewonski and Anderson, 1981].

[56] The 60-km, constant depth cross section (Figure 11) is through the uppermost mantle in most of the region but still through the lower crust below Tibet (Figure 2), hence the very low velocities there. Because we inverted simultaneously for S velocities and Moho depths, the 40–60 km thick crust in central China will affect mantle velocities on the 60-km image only if and where our crustal model (Figure 7) is in error. The velocities on the 100-km cross section correlate with the crustal thickness very weakly, except beneath the 70–80 km deep Tibetan Moho. By 150 km the trade-off is negligible.

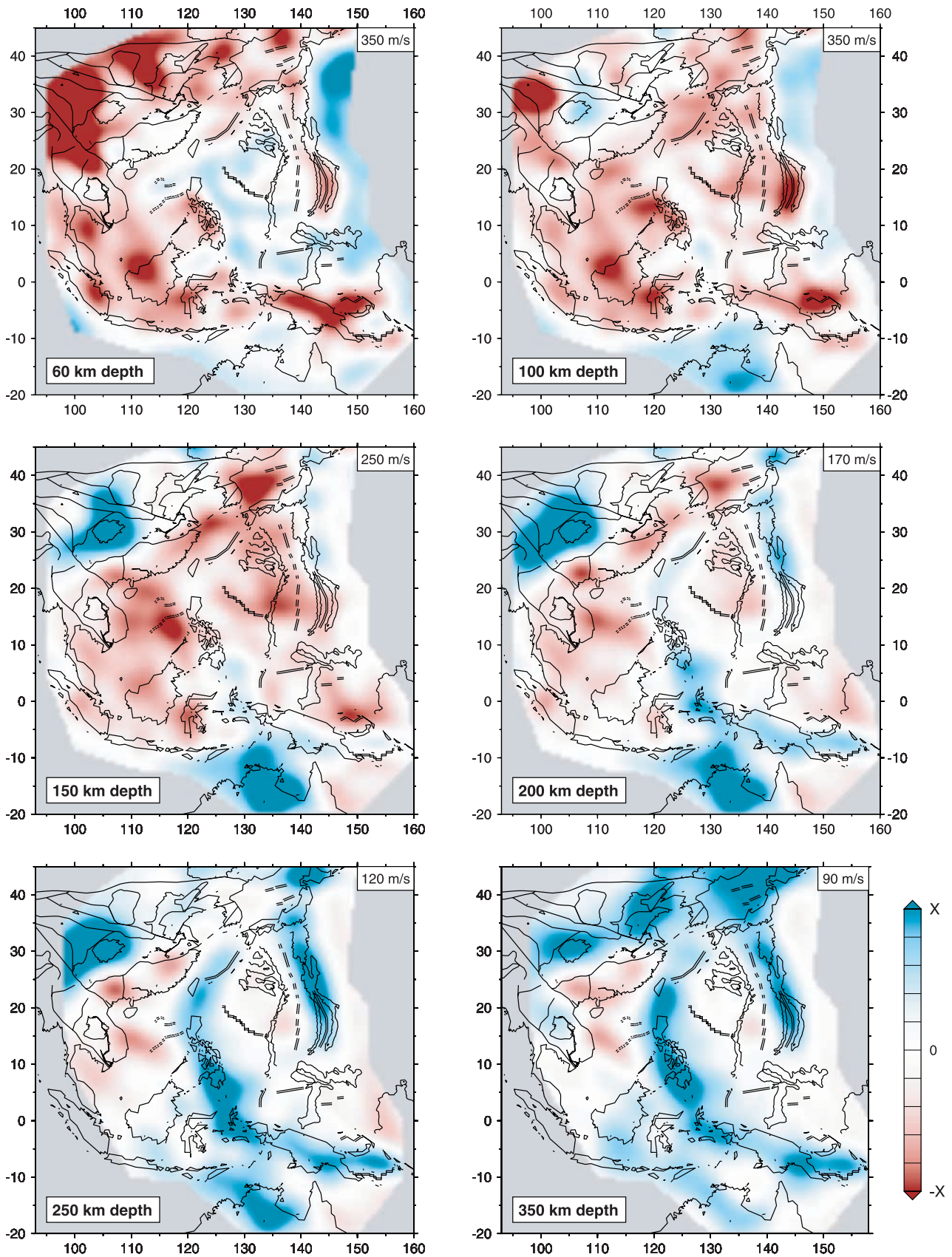


Figure 11. Constant depth cross section through the SE Asia-western Pacific upper mantle at six depths. Tectonic boundaries are as in Figure 2. The limits of the color scale X are shown in the upper right corner of each plot. The reference velocities are 4.4 km/s at 60–200 km, 4.48 km/s at 250 km, and 4.68 km/s at 350 km depth.

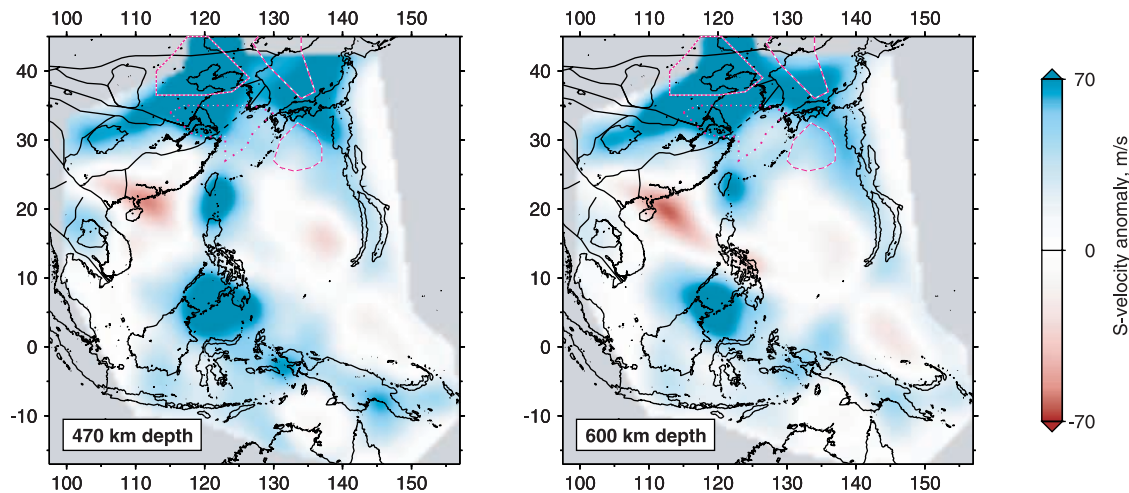


Figure 12. Constant depth cross section through the SE Asia-western Pacific transition zone at two depths. Tectonic boundaries are from Figure 1. The reference velocities are 5.14 km/s at 470 km and 5.35 km/s at 600 km depth. Dashed and dotted red lines enclose the four regions from *Tajima and Grand* [1998], three with high velocities (dashed) and one with normal velocities (dotted).

[57] The main features of the model as a whole are the range and the scale of shear velocity variations. Figure 13 displays the range of S velocity values as well as velocity profiles at a few locations where extreme anomalies are detected. Down to 75 km the largest contrast is between the slow crustal rock of the Tibetan crust and the faster mantle rock elsewhere (Figure 11). The lowest velocities in the 80–110 km depth range are still beneath Tibet. If Tibet is excluded, the lowest velocities at this depth are beneath the active spreading centers in the Bismarck and Mariana Basins, where S velocity reaches a minimum in the 80–110 km depth interval.

[58] The minimal values below 120 km are beneath two regions of Cenozoic intraplate volcanism. South central Sea of Japan has the lowest velocities in the 130–190 km depth range (high velocities at 300–400 km indicate the presence of subducting Pacific lithosphere). Below 200 km, the lowest velocities in the model are beneath southeastern China and eastern Indochina. A low-velocity feature beneath the Hainan Island and the South China Sea extends down to the 660-km discontinuity (Figure 12).

[59] The highest velocities in the 90–200 km depth range are beneath two Precambrian cratons, in south China and north Australia. The cold lithosphere descending beneath subduction zones might in fact be similarly fast, but the magnitude of the anomalies within the relatively thin (<100 km) subducting slabs is underestimated on the images with 400-km resolution (Figure 10).

[60] In general, shear velocity varies the most in the upper portion of the mantle, down to 150 km depth. If Tibet is excluded, the range is 17–18% in the 90–150 km depth interval. At greater depths, the model underestimates the magnitudes of anomalies, which contributes to the apparent decrease in the range of velocity variations. This underestimation, however, cannot account for all of the decrease. According to checkerboard resolution tests (Figure 8), the anomaly magnitude at 300 km depth is underestimated by a factor of 1.5 to 3. Yet, the range of observed S velocity variations drops from 18% at 150 km to about 5% at 300 km

depth, which implies that heterogeneity does decrease below 150–200 km. Using 2 for the amplitude reduction factor, we estimate the range of S velocity variations at 300 km at 10%.

6. Continental Lithosphere

[61] The mantle above the 410-km discontinuity usually contains the lithosphere, underlain by the asthenosphere. The definition of the lithosphere-asthenosphere boundary depends on the criteria used, particularly beneath continents. *Griffin et al.* [1998b] suggest a combination of two criteria. According to one [*McKenzie and Bickle*, 1988] the transition is at the bottom of the thermal boundary layer, where a conductive geotherm (in the lithosphere) changes to an adiabatic one (in the asthenosphere). According to the other (equivalent to the first if the system is in dynamic equilibrium), the boundary is between the stable, relatively depleted lithosphere and connecting, more fertile asthenosphere. This combined definition adopted, studies of mantle xenoliths suggest that the base of the lithosphere beneath cratons worldwide is in the 150–250 km depth range [*Griffin et al.*, 1998b].

[62] Seismic lithosphere is defined as a “fast” lid on the top of a low-velocity zone, identified as the asthenosphere. The pattern is universally observed beneath the oceans, but is often less pronounced beneath the continents. Seismic data suggest that high-velocity anomalies under some of the Archean cratons extend down to 300 km and possibly deeper [e.g., *Jordan*, 1975]. According to *Jordan* [1975, 1988], the continental tectosphere in the subcratonic mantle is significantly colder than the average in the depth range. Yet, because of a compositional difference the cratonic “roots” are less dense than the oceanic upper mantle and therefore are buoyant.

[63] In some locations beneath the cratons of SE Asia and north Australia we detect the presence of the high-velocity roots. Their thickness varies laterally on a scale of hundreds of kilometers, possibly smaller. In other cratonic locations, high-velocity anomalies are absent. However, the lid-LVZ pattern, a faster layer on top of a slower one, is often present

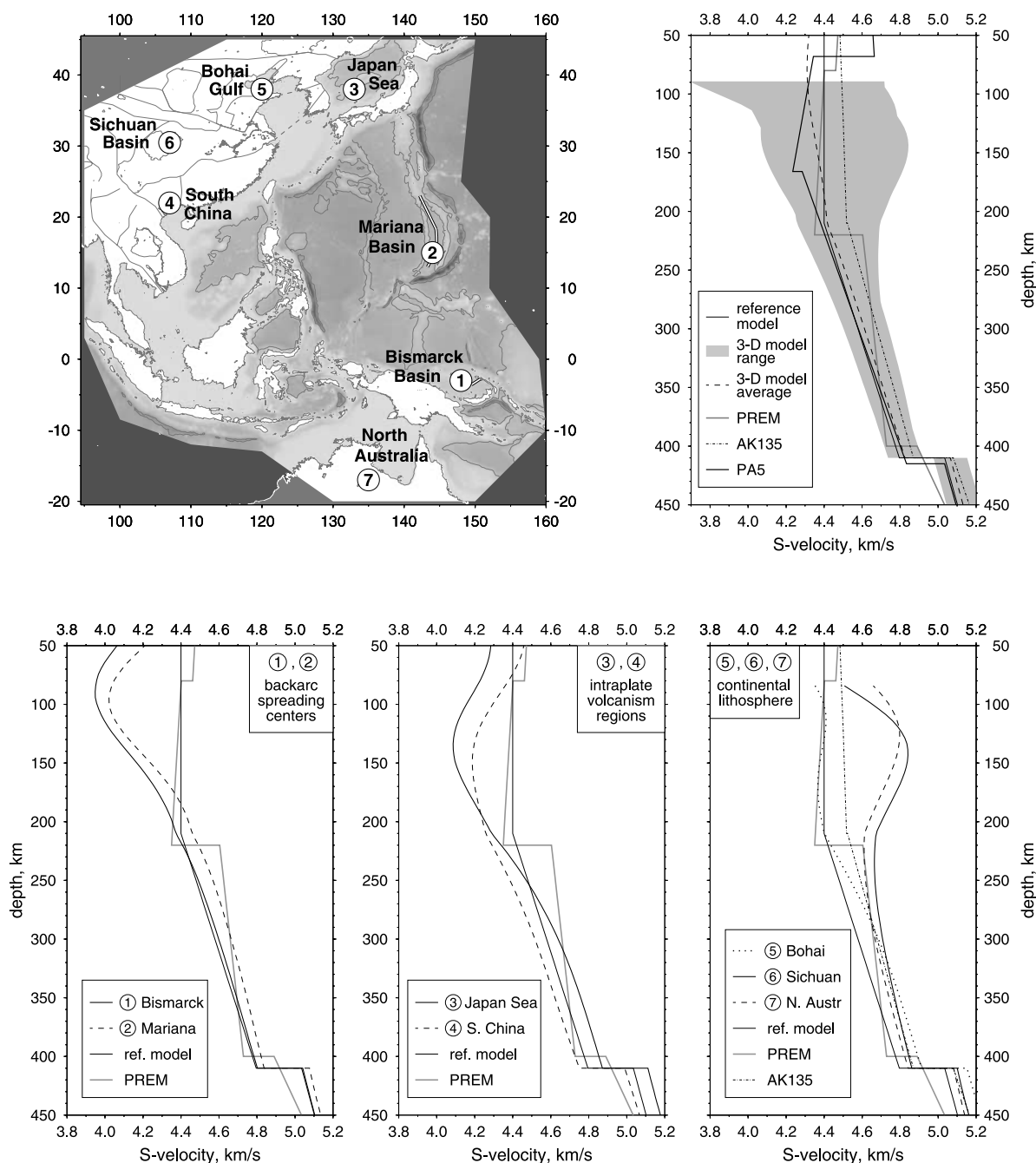


Figure 13. (top left) Region covered by our model and the locations of the velocity profiles shown below. (top right) Range of S velocity variations in the 3-D model (grey shading) and the reference and average velocity profiles, compared with PREM [Dziewonski and Anderson, 1981], AK135 [Kennett *et al.*, 1995], and PA5 [Gaherty *et al.*, 1996]. PREM and PA5 are recomputed at the reference period of 50 s, using the attenuation profiles of each model. (bottom) One-dimensional profiles through our 3-D model at selected locations of extreme S velocity anomalies: the active spreading centers in (left) the Bismarck (1) and Mariana (2) back-arc basins; (middle) circum Sea of Japan (3) and south China (4) regions of intraplate basaltic volcanism; and (right) eastern Sino-Korean (5), Yangtze (6), and north Australian (7) cratons.

even when both layers are relatively slow (e.g., profile 5 in Figure 13). The depth of such “average-slow”-“slower” transitions varies from about 70 to 150 km.

6.1. Sino-Korean Craton

[64] At the 100 km depth (Figure 11), the low velocities in the center of the craton are probably related to the

widespread Cenozoic rifting and magmatism. At 150–200 km, S velocities beneath the North China Block are close to our reference value of 4.4 km/s, still rather low in a continental setting. Beneath the Archean cratonic nucleus under the Ordos Basin (Ordos Plateau) and to the west and north of it, the velocities are somewhat higher. Since the basin is surrounded by active or recently active rifts, we

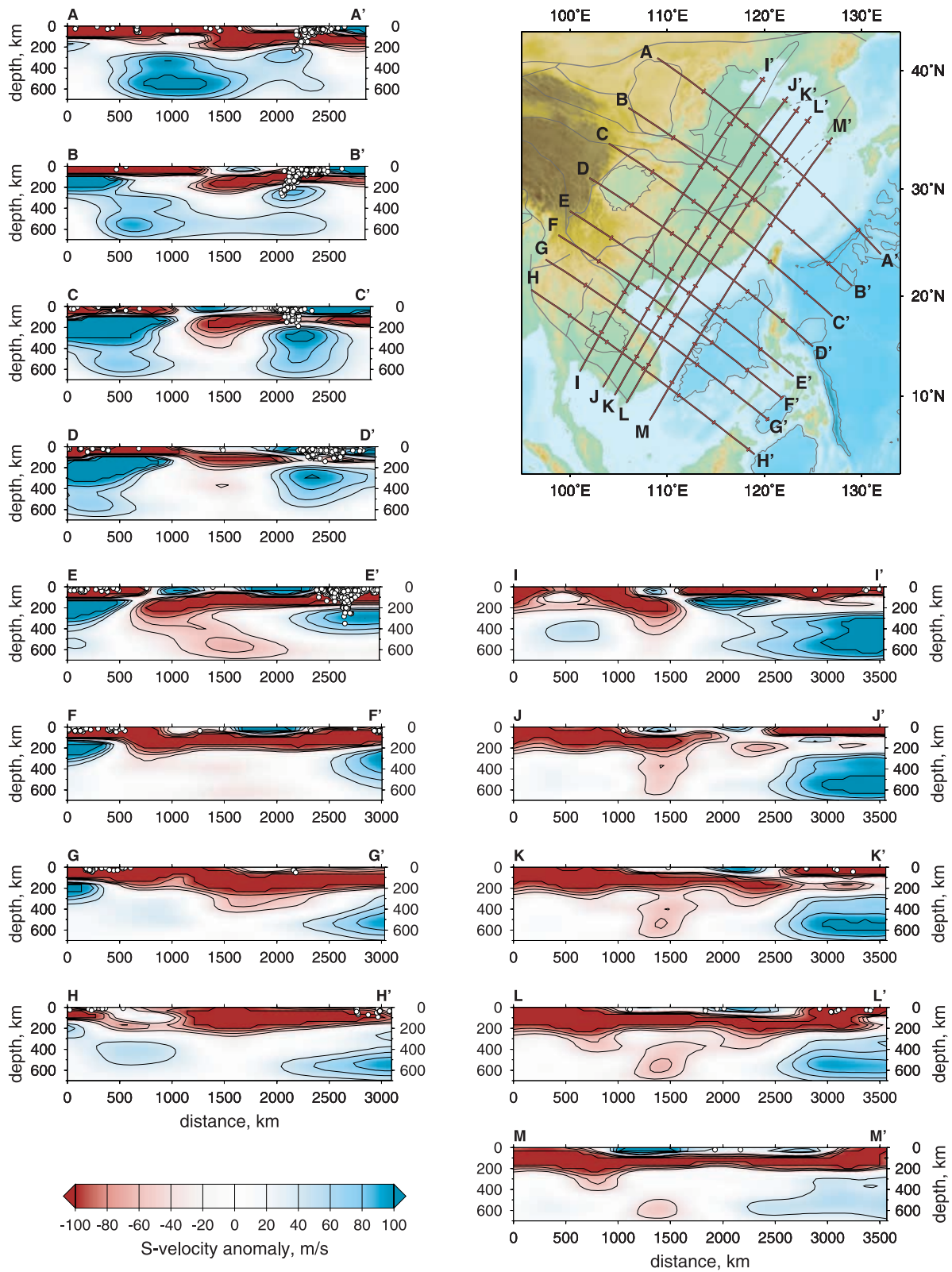


Figure 14. Vertical cross sections through the model across SE Asia. Contours are at ± 40 , ± 60 , ± 80 , and ± 100 m/s. Tick spacing on the section lines on the map is 500 km. Earthquake hypocenters are from the catalogue of Engdahl *et al.* [1998].

may observe an average of high velocities beneath the relatively small basin and low velocities around it. The high-velocity root beneath the basin extends down to 200–250 km (Figure 14, B-B').

[65] The eastern Archean nucleus of the craton (around the Bohai Gulf) also has velocities close to 4.4 km/s in the upper 200 km. A major Cenozoic rift system goes through the Bohai Gulf (Figure 2); again, our velocity value might be an average over small-scale faster and slower features. *S* velocity appears to decrease from 4.4–4.45 km/s at 110–120 km to about 4.35 at 170–200 km (Figure 13); the bottom of the lithosphere can be inferred to be at around 140–150 km depth.

[66] Studies of mantle xenoliths of different ages [Griffin *et al.*, 1998b; Menzies and Xu, 1998] suggested that an Archean 200-km-thick keel beneath north China has been largely eroded and replaced with Phanerozoic material during the last 500 m.y. Griffin *et al.* [1998a], however, point out that simple heating (“thermal erosion”) may not be a plausible mechanism for the destruction of an Archean keel, the latter becoming only more buoyant once heated. Instead, they favor the scenario proposed by Yuan [1996], suggesting that the asthenospheric material has risen through the pulled-apart lithosphere in narrow linear zones, so that at present small-scale blocks of Archean mantle alternate with vertical zones of asthenospheric mantle. Our model is consistent with this scenario. The seismic lithosphere that we observe beneath the eastern Sino-Korean Craton is thick and rather slow at the same time (Figure 13). Since the values in the model are averages over 400 km or so, alternating fast and slow features 50–100 km wide would be expected to produce the apparent average-low velocities that we observe. The presence of asthenospheric material at shallow depths may not require a total removal of the Archean material below 80 km [Griffin *et al.*, 1998b; Menzies and Xu, 1998] but simply indicate the presence of the rising asthenospheric material, which with time will change the bulk composition of the relict Archean blocks through mixing and metasomatism [Griffin *et al.*, 1998a]. These processes may be already complete below about 150 km, the apparent depth of the lithosphere-asthenosphere boundary in our model.

6.2. Songliao Basin

[67] The western half of the Songliao Basin (to the north of the Sino-Korean Craton) is underlain by a high-velocity anomaly. The root is also observed to the west of the basin. This observation is consistent with the result of Zhang *et al.* [1998], who analyzed the potassic volcanic rocks and mantle xenoliths from Northeast China and concluded that the Songliao Block is an Archean-early Proterozoic mantle terrane that extends beyond the present boundary of the basin, below the mountains to the west.

6.3. Yangtze Craton

[68] The high-velocity root beneath the western Yangtze Craton is the fastest anomaly in the region in the 120–300 km depth range (Figures 11 and 13). Shear velocity reaches the maximum (4.8 km/s at 120–170 km) beneath the Sichuan Basin, the Archean core of the craton (Figure 13).

[69] The Yangtze continental root appears as a fast anomaly in some of the recent global tomographic models

[e.g., Van Heijst *et al.*, 1999]. The resolution of our tomography allows us to determine the extent of the anomaly and its magnitude with higher accuracy. The high-velocity root underlies the part of the Yangtze Craton west of 110°E (Figure 11). Between 200 and 300 km the elongated root is almost 1800 km long (SW-NE) and 1000 km wide (NW-SE). The southeastern boundary of the anomaly coincides with the boundary of the craton on the surface. In contrast, on the west and northwest the root extends beyond the cratonic boundaries by about 500 km. On the north it reaches the Archean Ordos Basin in the Sino-Korean craton but seems much faster than the Ordos's root.

[70] At the western edge of our study region (southwest of Yangtze), we may be sampling the fast lithosphere of the Indian shield. If so, it must be adjacent to the Yangtze high-velocity root. A future high-resolution study with a target region including both Tibet and central China would be necessary to determine the spatial relationship between the Yangtze and Indian continental lithosphere.

[71] At 100–150 km, a low-velocity anomaly underlies northeastern Tibet, west-northwest of the craton. In this location, Curtis and Woodhouse [1997] mapped the lowest *S* velocity beneath the Tibetan Plateau in the 115–185 km depth range. At 200 km, the fast Yangtze anomaly expands to below the area.

[72] The fold belts to the west and northwest of the Yangtze Craton are complex and include a number of microcontinents, possibly ancient [e.g., Li, 1998]. The extent of the Yangtze anomaly might be due to their fast lithosphere, accreted to the root of the craton or situated close enough to it to be indistinguishable on the image. It seems more likely, however, that we observe a single Yangtze root of ancient origin. If this is the case, the deep rigid continental root must have underthrust the composite terranes to the northwest during the Triassic-Jurassic suturing.

[73] The high-velocity root extends down to about 300 km, deeper beneath the Sichuan Basin and shallower (150–200 km) near the eastern margin of the craton (Figure 14, C-C' and D-D'). Below Sichuan and to the northeast of it, a high-velocity anomaly is also present in the transition zone (Figures 12 and 14).

6.4. Southeast China and Indochina

[74] Beneath most of the East China Foldbelt, lithospheric *S* velocities are close to the average (4.4–4.5 km/s). Low-velocity zone begins at 50–80 km. In Indochina, the average velocity (4.4 km/s) lithosphere of the Khorat Basin and the area to the west bottoms at 120–150 km (Figure 14, H-H'). In the rest of Indochina, the negative velocity gradient that could be interpreted as the lid-LVZ boundary is small or absent.

[75] Sites of abundant Cenozoic intraplate volcanism are located in the northeastern corner of the East China Foldbelt (Figure 2), south China including the Hainan Island, and eastern Indochina. Prominent low-velocity anomalies underly these locations at 150 km and deeper. They clearly stand out against the background of the low-velocity zone at 200 km and persist down to 350–400 km depths, where *S* velocities are normal beneath most of the region (Figures 11, 12, and 14). The anomaly beneath south China and Hainan

extends down to the 660-km discontinuity under the South China Sea.

7. SE Asia's Transition Zone (410–660 km)

[76] A major high-velocity anomaly occupies the transition zone (TZ) beneath the eastern Sino-Korean Craton (Figure 12). It extends north beneath the Songliao Basin and may continue outside the region sampled by our data. It is the fastest anomaly on our TZ images, up to 2–2.5% fast in both the upper and lower TZ. According to resolution tests, the magnitude of an anomaly of this size in this location may be underestimated a factor of 1.5–2.5; the maximum magnitude (beneath the Bohai Gulf) is thus in the 3–6% range.

[77] *Tajima and Grand* [1998] studied the fast TZ anomalies in this area using triplicated regional *P* waves. TZ structure was constrained in four separate subregions shown in Figure 12, three with high (northeast China, Sea of Japan, and northern Philippine Sea) and one with normal (East China Sea and Yellow Sea) velocities. Using a very different data set, we find a similar pattern for *S* velocities, except that our normal velocity region beneath the east China Sea does not continue so far west (Figure 12).

[78] The fast anomaly beneath NE China extends from 350–400 km down. High velocities beneath the Songliao Basin may indicate Pacific lithosphere subducted at the Japan Trench. The part of the anomaly south of the Bohai Gulf may require a different explanation, because it is separated from the Pacific slab under the northern Philippine Sea by a region of normal TZ velocities beneath the East China Sea. The anomaly might indicate the trailing fragments of a subducted lithospheric slab, similar to the Farallon slab in the TZ beneath the western United States [*Van der Lee and Nolet*, 1997a]. If this is the case, the slab was subducted some time in the Cenozoic at a trench along or near the continental margin, possibly the Ryukyu Trench (Figure 14, A-A'), where subduction is relatively slow at present. Recent *P* velocity models show fast anomalies in approximately the same locations in NE China [*Bijwaard et al.*, 1998; *Kárason and Van der Hilst*, 2000]. According to the models, the high *-P* velocity anomalies continue across the 660-km discontinuity into the lower mantle, which suggest that they correspond to cold lithospheric slabs passing through the TZ on their way down.

[79] The NE China fast anomaly appears to continuously extend southwestward, under the northern and northwestern Yangtze Craton, as far as the Sichuan Basin. The structure here is not an artifact of smearing, either from above or from the northeast (Figure 15). The whole mantle models cited above agree with one another both on the presence of high-velocity features in this location (although not on their shape) and on the absence of anomalies in the uppermost lower mantle beneath. This central China anomaly may thus be of different origin, compared to the one on the northeast.

[80] The high-velocity anomaly in the upper TZ beneath Indochina (Figures 12 and 14, H-H') probably indicates the lithosphere subducted at the north-south trench west of Indochina. A slow anomaly is present in the TZ beneath

Hainan and the South China Sea. Farther east and south, the fast anomalies beneath the western Pacific island arcs correspond to the remnants of recently subducted oceanic lithosphere [*Widiyantoro and Van der Hilst*, 1997; *Bijwaard et al.*, 1998; *Kárason and Van der Hilst*, 2000].

8. SE Asia's Margins

8.1. Circum South China Sea Region: The Hainan Plume?

[81] Two regions of Cenozoic intraplate volcanism in the South China Sea region (in the Hainan Island area and in eastern Indochina) are underlain by low velocities down to 350-km depth (Figure 11). Near Hainan, a continuous anomaly reaches the lower TZ (Figure 14). An unresolved gap in the low-velocity column might exist near 300–400 km but is unlikely to exceed 150 km in thickness (Figure 16). The sample seismogram in Figure 3 is one of those sensitive to the Hainan anomaly.

[82] The low-velocity feature appears to be elongated in the TZ (Figure 12), wider in the northwest-southeast direction. Resolution tests (Figure 8) show that this shape may be partly due to smearing; the actual anomaly may be less elongated (in the map view). The width of the anomaly on the image is 400–600 km (southwest-northeast), similar to the tomographic resolution length (400 km), so that the actual anomaly in the Earth may be quite narrow. It is not clear whether the deep part of the Hainan anomaly has any relationship with the shallower low-velocity feature beneath Indochina or the similar one beneath eastern China (Figures 11 and 14).

[83] The Cenozoic basalts in the circum South China Sea region, particularly in Hainan, display the eruption morphology and isotopic ratios typical of the hot spot volcanism [*Tu et al.*, 1991], the latter commonly associated with deep-mantle plumes. Whether the basalts do have a deep mantle origin has been a matter of much debate, and a number of alternative scenarios have been proposed [e.g., *Flower et al.*, 1998; *Smith*, 1998]. Our results indicate that the enriched basalts may indeed come from a great depth. The high-resolution images show a subvertical plume-like structure throughout the depth range of the model, i.e., the upper mantle.

[84] The lower mantle below SE Asia seems to be dominated by downwellings, originating at subduction zones. Whole mantle tomography, however, shows that the deep mantle beneath the region is populated by more than just sinking slabs. In particular, most of the recent *S* and *P* velocity models display low velocities in the lower mantle beneath south China and Indochina, from 660 down to about 2000 km [e.g., *Su et al.*, 1994; *Bijwaard et al.*, 1998; *Van Heijst et al.*, 1999; *Kárason and Van der Hilst*, 2000]. Below 2000 km, current global models disagree: some show one extensive fast anomaly beneath all of the SE Asia; others show alternating small-scale fast and slow features [*Castle et al.*, 2000; *Kárason and Van der Hilst*, 2000]. None of the models resolves a continuous narrow plume-like structure, whether across the whole mantle or down to 2000 km. Perhaps, this is not to be expected, given the limits of resolution. However, the presence of low velocities in the lower mantle beneath the South China Sea region represents another argument for the existence of

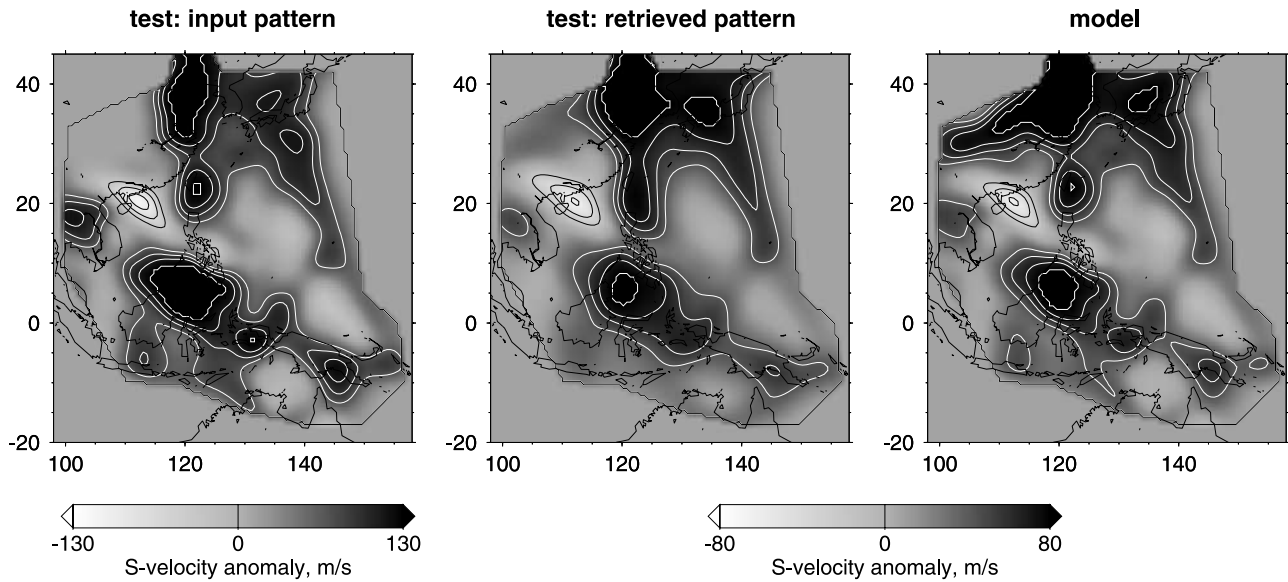


Figure 15. A resolution test for the high-velocity anomaly in the transition zone beneath central China. The cross sections are at 530 km depth. Everywhere except for the central China TZ (left) the input test pattern is such that (middle) the output pattern is very similar to (right) the actual model, so that the test also illustrates the reduction in the anomaly magnitude due to overdamping in mid-TZ. In the input, there is no anomaly west of 115°E, north of 25°N and deeper than 350 km (the high-velocity Yangtze Craton above is present). The effects of smearing as seen in the output are small and cannot be responsible for the observed anomaly. The contours are at $\pm 40\%$, $\pm 60\%$, $\pm 80\%$, and $\pm 100\%$ of the grey scale limit.

a plume. If this is the case, the images presented here show the upper mantle part of the deep-mantle Hainan plume.

[85] On the south, the South China Sea reaches Borneo, southern part of which has also been considered a location of hot spots [Burke and Wilson, 1976]. We do not detect a substantial anomaly there but image a prominent slow feature beneath the northwestern part of the island. This area comprises fold belts and the terranes

accreted as a result of Cenozoic subduction along the coast [Bénard *et al.*, 1990]. The anomaly continues offshore (beneath the Luconia microcontinent) but does not extend below 200 km.

8.2. Circum Sea of Japan Region

[86] The Circum Sea of Japan Alkaline Rock Province [Nakamura *et al.*, 1989] contains many sites of Cenozoic

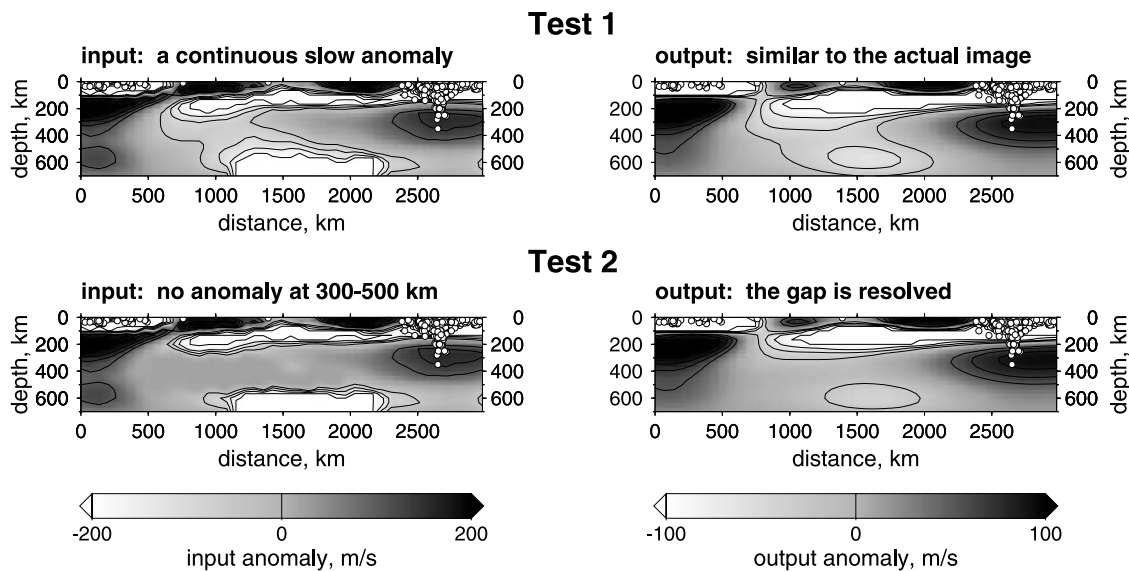


Figure 16. Two resolution tests for the “plume” structure. The location of the cross section is that of E-E’ in Figure 14. The input pattern (bottom) of test 2 differs from that (top) of test 1 only by the absence of any anomaly at 300–500 km in the vicinity of the plume. The actual anomaly in the model (Figure 14, E-E’) can be reproduced in the tests if the input plume anomaly is continuous (test 1). A 200-km gap in the plume structure can be resolved (test 2). The contours are at $\pm 40\%$, $\pm 60\%$, $\pm 80\%$, and $\pm 100\%$ of the grey scale limit.

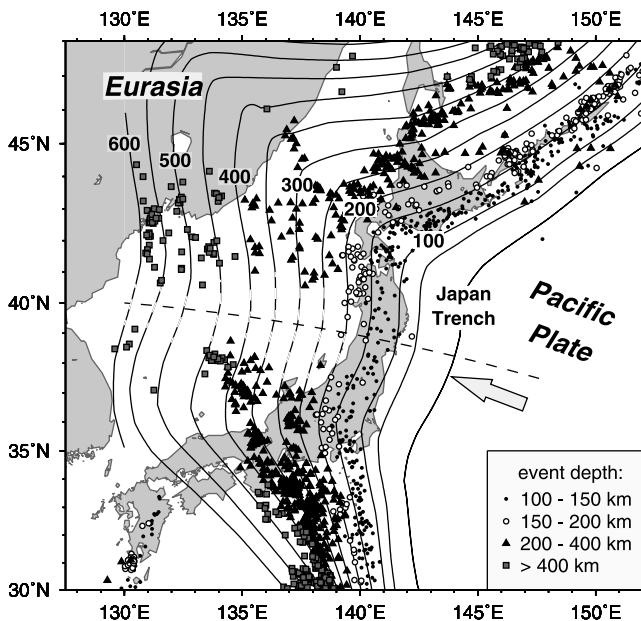


Figure 17. Deep seismicity in the Sea of Japan area, from the catalogue of *Engdahl et al.* [1998]. A seismicity gap is observed near 39–40°N. Solid lines show the slab contours at a 50-km depth interval from *Gudmundsson and Sambridge* [1998]. The contours are approximately at the top of the slab's seismogenic zone; in the seismicity gap area they are drawn with dashed lines. The bold dashed line is approximately through the middle of the gap. The arrow shows the direction of motion of the Pacific Plate relative to Eurasia.

basaltic volcanism; once more, a mantle plume has been one of the proposed explanations.

[87] Recently, *Zhao et al.* [2000] has combined a global delay time data set with regional data from the J array in Japan and observed a prominent slow anomaly beneath central Japan. The feature extended from 260 km depth (beneath the subducting Pacific slab) down to about 1800 km and was interpreted as a hot deep-mantle plume, producing local warming, thinning, and increased dehydration of the slab.

[88] Here we used the resolving power of multimode surface waves and constrained the structure in the shallower mantle beneath the Sea of Japan, a domain poorly sampled by *P* delay data sets. Beneath the south central part of the sea, we find shear velocities below 4.1 km/s in the 130–190 km depth range. A domain of hot, partially molten mantle rock in this location could be the source region of the basalts that have been erupting in the province. The chemistry of the alkaline rocks is similar to that of the ocean island basalts [*Nakamura et al.*, 1989], possibly pointing to a deep-mantle origin. But could the shallow low-velocity region have any relationship with the plume-like anomaly imaged by *Zhao et al.* [2000]?

[89] It seems very unlikely that a relatively thin plume could melt a “hole” through the old Pacific lithosphere that is subducting at the Japan Trench at a rapid rate. Buoyant melt, however, might penetrate through the lithospheric rock in the form of thin dykes, given the extensional regimes in

the lower part of the slab as it “unbends” (at 100–150 km depth) and in the upper part where it “bends”, approximately above. An interesting and possibly relevant observation is illustrated by Figure 17. According to the hypocenter catalogue of *Engdahl et al.* [1998], there is a gap in deep seismicity at the Japan subduction zone near 40°N, with no earthquakes deeper than 200 km, and very few deeper than 150 km. The gap is about 150–200 km wide and strikes approximately perpendicular to the trench, also close to the azimuth of the plate convergence, as if the slab was somehow modified to become aseismic in one particular location beneath Japan. Outside the gap, the slab is highly seismic (Figures 17 and 18, A-A', B-B').

[90] Our 400-km resolution would not allow the detection of a 100–200 km wide part of the slab with relatively low velocities or even a narrow slab window if it existed. Perhaps, the best way to investigate the structure near the apparent seismicity gap would be with short-period, delay time data. More extensive hypocenter catalogues as well as earthquake source mechanisms could provide additional information.

8.3. Marginal Basins and Subduction Zones

[91] One of the most intriguing features that we observe beneath the back-arc basins of the western Pacific is the low-velocity anomaly beneath the Central Basin Ridge in the West Philippine Basin (Figures 2 and 11, 100 and 150 km depth). Most likely a narrow (<100 km) feature, it underlies a spreading center extinct for more than 30 m.y. The anomaly was detected previously by *Lebedev et al.* [1997] and *Nakamura and Shibutani* [1998]; it is unlikely to be simply due to the younger age of the lithosphere near the ridge [*Lebedev et al.*, 1997]. The anomaly indicates that partial melt may still be present beneath the ridge. Another low-velocity anomaly is found near the extinct spreading center in the South China Sea (Figure 11). This anomaly is larger in magnitude but is not centered directly beneath the ridge axis.

[92] Figure 18 shows vertical cross sections across two major subduction systems in the region. On A-A'–D-D' the Pacific plate is seen subducting beneath Japan and the Philippine Sea. In agreement with the deep-seismicity patterns and the images from high-resolution *P* delay tomography [e.g., *Van der Hilst et al.*, 1991], the subduction angle steepens from the Japan to the Izu-Bonin and Mariana Trenches. No significant anomaly is observed beneath the Yap and Palau Trenches (7°–10°N, Figure 11), where subduction has largely ceased because of the arrival of the massive Caroline Ridge.

[93] The Sunda-New Guinea zone of convergence is dominated by the subduction of the Indo-Australian lithosphere. Beneath New Guinea (Figure 18, E-E'–H-H'), the northward subduction has stopped because of the collision of the Australian continent with the island arc that currently forms northern New Guinea.

9. Discussion

9.1. Range of Shear Velocity Variations

[94] In a recent global-scale analysis, *Ekström* [2000] compared the shear velocity profiles that averaged over different tectonic areas, such as young and old oceans,

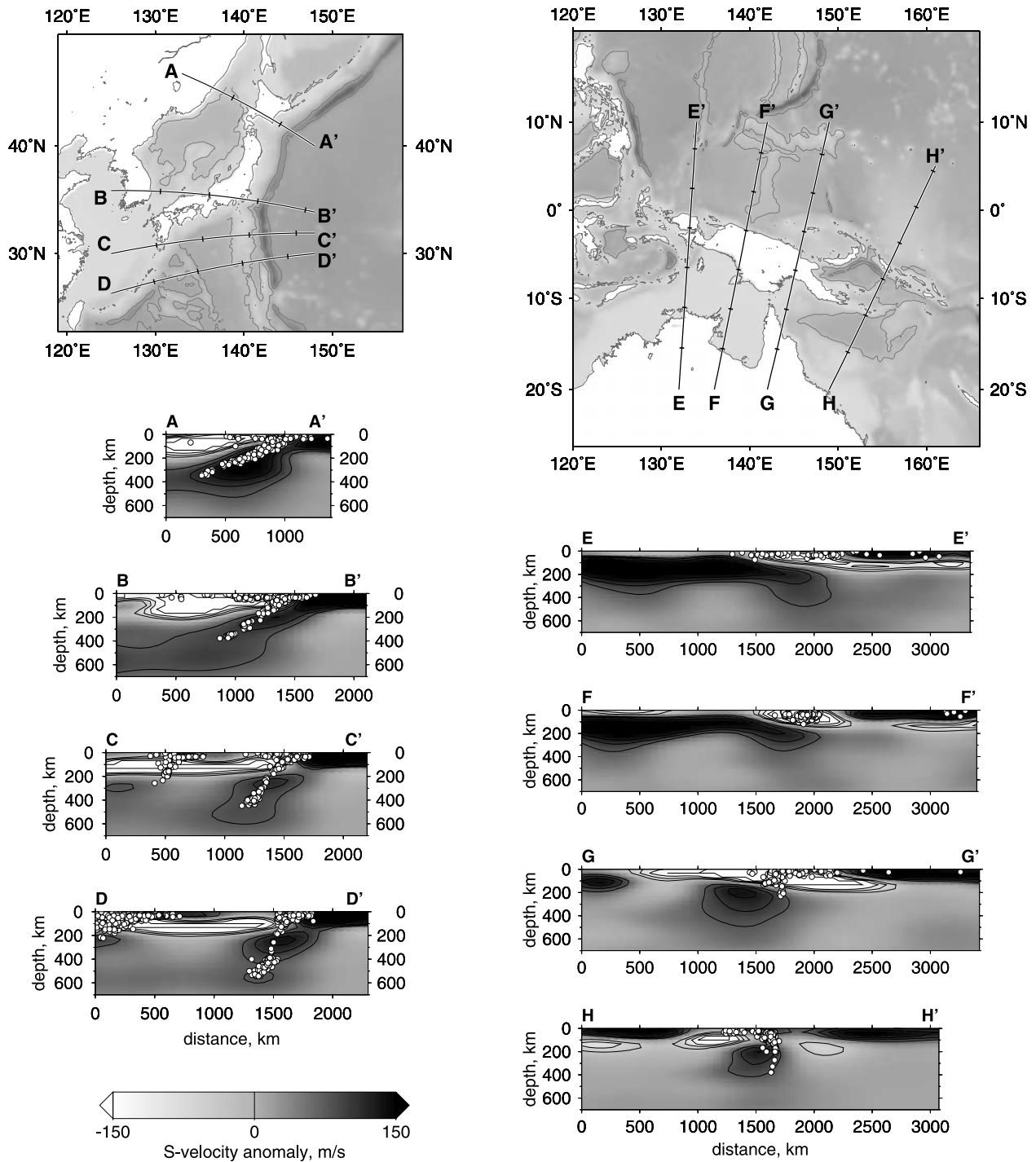


Figure 18. Vertical cross sections through the model across the Japan-Izu-Bonin subduction system (A-A'–D-D') and across the New Guinea-Solomon zone of convergence (E-E'–H-H'). Contours are at ± 60 , ± 90 , ± 120 , and ± 150 m/s. Tick spacing on the section lines on the maps is 500 km. Hypocenters are from Engdahl *et al.* [1998].

continents, and stable continents. The range of the variations defined by the average profiles was the widest at 100–150 km and decreased below, a pattern consistent with the one observed here (Figure 13). According to the images of Ekström [2000], the full range of S velocity values in the global tomographic model [first published by Ekström and Dziewonski, 1998] was about 13% at 150 km depth, narrower than the 18% obtained here.

[95] The range of velocity variations is related to the tomographic resolution. If the resolution length is larger than the size of actual anomalies, their magnitude is underestimated. Some of the slowest features of our model (back-arc spreading centers and intraplate volcanic regions) are absent in the lower-resolution global model. While detecting the anomalies, our tomography still underestimates their magnitude: the width of a back-arc spreading center or the

thickness of a subducting slab are probably less than 100 km, smaller than our 400-km resolution length. The observed 18% range should thus be considered a lower estimate. Previous regional studies with lateral resolution comparable to ours retrieved similar peak-to-peak amplitude of S velocity variations [Van der Lee and Nolet, 1997b; Simons *et al.*, 1999; Frederiksen *et al.*, 2001]. In the middle and high-velocity portions of the range, the primary cause of the variations is probably thermal heterogeneity; in the low-velocity portion partial melting and the presence of volatiles can also be important [Sobolev *et al.*, 1996; Goes *et al.*, 2000].

9.2. Cratonic Lithosphere

[96] We observe the highest S velocities beneath the Archean Sichuan Basin, within the high-velocity root of the Yangtze Craton. The fast anomaly extends down below 300 km. The decrease of the shear velocity between 150 and 200 km (Figure 13) is partly due to the inversion over-damping below ~ 150 km, so that the magnitude of the negative velocity gradient at 150–200 km is not well constrained. The maximum S velocity beneath Sichuan is detected at 140–150 km depths and reaches 4.84 km/s.

[97] Resolution tests suggest that the anomaly is not likely to be overestimated in magnitude. The test with the actual model as an input pattern underestimated the Sichuan anomaly in the output (4.74–4.77 km/s at 130–160 km depths, down from 4.81–4.84 km/s). Because azimuthal anisotropy is unlikely to cause a bias exceeding 1%, S velocity does appear to reach ~ 4.8 km/s within the Sichuan root.

[98] We find similarly high velocities (up to 4.8 km/s) beneath northern Australia (Figures 11 and 13); high-velocity lithosphere bottoms at a shallower depth of about 250 km beneath most of that region (Figure 18). Simons *et al.* [1999] performed multimode surface wave tomography of the Australian continent and found the same S velocity values (around 4.8 km/s) and the same lithospheric thickness in the location of the profile 6 of Figure 13 in northern Australia (F. Simons, personal communication, 2000). S velocity up to 4.8 km/s was also detected by Van der Lee and Nolet [1997b] beneath a part of the Archean Superior Province in North America at 120–130 km depths.

[99] Griffin *et al.* [1998a] estimated that the low-density Archean lithosphere can be positively buoyant while up to 600°C cooler relative to the asthenosphere; this would translate to a feasible thermal shear velocity increase of up to 5%. They also argued that the Archean continental lithosphere is sufficiently depleted in basaltic component (as well as low in Ca/Al and Mg/Si) to produce S velocities as much as 3% higher than those in the Phanerozoic upper mantle at the same conditions. Other workers, however, agree on the velocity variations of compositional origin up to 1% only [Nolet and Zielhuis, 1994; Sobolev *et al.*, 1996; Goes *et al.*, 2000].

[100] One more contribution to the apparent magnitude of the cratonic anomalies comes from anomalously low reference velocities. Our study region contains a few stable continental blocks, but the average velocities in the upper 200 km of the mantle are lowered because of the abundance of active or young marginal basins (very slow due to partial melting and the water from the subducting oceanic crust) and tectonically active continental regions. The global-

average asthenospheric S velocities (e.g., in PREM) are biased toward low oceanic values; the low-velocity zone beneath oceans is thought to be caused by either partial melting or the presence of volatiles [e.g., Hirth and Kohlstedt, 1996]. Thus the high-velocity anomalies that we observe within the cratonic lithosphere are partly due to its low temperature and anomalous composition but also due to the fact that the reference (average) values are low as a result of other, completely different processes. If we assume “normal” S velocities to be around 4.5 km/s as in AK135 (a conservatively low value), then a combination of the thermal (5%) and compositional ($\sim 1\%$) effects can account for the ~ 4.8 km/s S velocities beneath cratons.

9.3. High-Velocity Anomalies in the Transition Zone

[101] The presence of recently subducted, cold oceanic lithosphere has been the best documented cause of fast anomalies in the TZ. Subduction in northwestern Pacific also provides a prime example of “slab deflection” at the 660-km discontinuity: according to high-resolution delay time tomography [e.g., Bijwaard *et al.*, 1998; Káráson and Van der Hilst, 2000], the lithosphere subducted at the northern Izu-Bonin Trench does not sink directly into the lower mantle but “flattens” in the TZ. The deflection cannot be attributed to a relatively young age of the lithosphere and insufficiently low temperatures in it, because the portions of the Pacific plate recently subducted at the trenches were more than 100 m.y. old. Instead, the phenomenon may be due to the migration (retreat) of the trenches [e.g., Van der Hilst and Seno, 1993]. The ultimate fate of the slabs that appear to be stagnant in the TZ is debated. There is no evidence, however, that the slab material stays there permanently. The P velocity models cited above show high velocities in the lower mantle below the northwest Pacific fast TZ anomaly, evidence for the descent of the slabs further down, after the deflection.

[102] Our observations beneath China show that there has to be a mechanism for the formation of long-term anomalous high-velocity domains in the TZ. While high velocities on the north of the study region may be attributed to recent subduction of oceanic lithosphere (consistent with high velocities observed in the uppermost lower mantle below), the fast anomaly in the TZ beneath the northwestern Yangtze Craton needs a different explanation. Three potential causes of the anomaly appear to be plausible: (1) oceanic lithosphere subducted anciently, (2) ultradeep continental roots, and (3) subducted continental lithosphere.

[103] 1. Are there portions of subducted oceanic lithosphere stagnant in the TZ? Central China’s high-velocity anomaly in the TZ is clearly not a result of recent subduction: there are no subduction zones nearby. The anomaly, however, could be caused by fragments of oceanic lithosphere subducted in the remote past, now stagnant in the TZ and still relatively cold. In the hot spot plate tectonic reference frame, there was a trench (striking approximately north-south) in the present location of east China at 50–70 Ma [Lithgow-Bertelloni and Richards, 1998]. In this reference frame, Eurasia has since migrated East, together with the subduction zones along its eastern margin. If we assume that the motion of China’s continental lithosphere was decoupled from that of the TZ beneath and that the latter remained stationary, then oceanic lithosphere could have

most recently descended into the TZ beneath the northwestern Yangtze Craton at that time, 50–70 Ma.

[104] We do not observe a vast anomaly in the TZ stretching east-west beneath all of the eastern China. Hence most of the oceanic lithosphere subducted at the trench has by now descended deep into the lower mantle. It is not clear why small portions of the large volume of subducted material would stay in the TZ and why they would form an elongated anomaly striking east-northeast. Still, the hypothesis has an advantage of explaining all SE Asia's TZ anomalies with one conventional mechanism (subduction of oceanic lithosphere).

[105] 2. Do continental roots extend into the TZ? The China's fast TZ anomaly stretches beneath three Archean cratonic nuclei: Songliao, eastern north China, and Sichuan. Below Songliao and Sichuan, high velocities can be seen in the whole 100–660 km depth range. Beneath the Bohai Gulf region, however, where the deep “root” is the fastest, high velocities are not observed in the upper 300 km of the mantle. As discussed above, Phanerozoic asthenospheric material is likely to occupy the 150–250 depth range in this location. If the TZ anomaly were indeed a part of the continental tectosphere, then the deep root would not be buoyant, contrary to the basic assumptions of the tectosphere theory.

[106] 3. Is there subducted continental lithosphere stagnant in the TZ? High velocities are present approximately along the northern boundary of the Yangtze Craton, prompting a possible link with the Triassic-Jurassic continental collision between the South and North China Blocks. Studies of the ultrahigh-pressure (UHP) rocks [e.g., *Liou et al.*, 2000] produced evidence for the Triassic subduction of some of the Yangtze continental crust and lithosphere. The UHP rocks are found in the Dabie-Sulu orogenic belt along the eastern part of the Yangtze-Sino-Korean boundary (approximately 32°N, 116°E to 37°N, 122°E, Figure 2). The UHP terranes consist mostly of crustal rocks and contain inclusions of diamond and coesite, suggesting that the rocks experienced pressures of more than 3 GPa. This can be explained by subduction of continental crust down to depths as great as 135 km [*Liou et al.*, 2000]. The underlying lithosphere subducted as well and must have stayed in the deep mantle after the detachment and exhumation of the buoyant crust.

[107] We hypothesize that the subducted continental lithosphere sank into the TZ, the descent assisted by the α - β transformation at the 410-km discontinuity. However, it could not proceed further down, possibly because of the “partial barrier” due to the negative Clapeyron slope of the phase transformation at the 660-km discontinuity. Because cratonic continental lithosphere is likely to be depleted in basaltic constituents and thus lighter than oceanic lithosphere [*Jordan*, 1975, 1988; *Griffin et al.*, 1998a], it is possible that, unlike oceanic lithosphere, it cannot penetrate into the lower mantle and is bound to stay in the TZ for hundreds of million years.

[108] The velocity anomaly is probably mostly due to remanent low temperature, given that a large mass of cold lithosphere accumulated in the TZ. For the heating time of 200 Ma the characteristic length of heat conduction is ~ 80 km (assuming the thermal conductivity $k = 10^{-6}$ m²/s), meaning that the temperature anomaly in the middle of a

160-km thick slab (infinitely wide) would decrease by about a factor of 2. The unknown shape and volume of the subducted lithospheric fragments would determine the actual present-day anomaly. If the thermally induced S velocity contrast had initially been 5% and by now dropped by a factor of 2.5–3.0, then the remaining lower-TZ anomaly would be 90–110 m/s. The anomaly in our model (~ 60 m/s) is underestimated in the lower TZ by a factor of 1.5–2.5, which suggests that the actual anomaly (90–150 m/s) can be attributed to the remanent low temperature. The anomalous composition of the subducted continental lithosphere may also play a role. If this hypothesis is correct, we observe continental lithosphere stagnant in the TZ for about two hundred million years. This phenomenon may account for the fast TZ anomalies beneath old orogenic belts in other parts of the world, including, for example, the UHP terrane near Maksutov, Kazakhstan [*Liou et al.*, 1996], underlain by high-velocity TZ according to the model of *Van Heijst et al.* [1999].

[109] We prefer the latter scenario for the origin of the anomaly, although it has to be noted that it does not explain why the UHP terranes do not extend to the western Yangtze Craton, as could be expected if continental lithosphere subducted along all of its northern-northwestern boundary.

10. Conclusions

10.1. Range of S Velocity Variations

[110] The observed peak-to-peak amplitude of S velocity variations is the largest (17–18%) in the upper 150 km of the mantle and decreases below. The highest anomalous velocities occur in the continental roots and subducting slabs. The lowest velocities above 120 km are beneath active spreading centers; from 120 to 660 km the lowest velocities are beneath regions of intraplate volcanism. Most of the fastest and slowest features are a few tens to a few hundreds of kilometers wide; the magnitude of the anomalies is underestimated by tomographic inversions; 18% is a lower estimate for the amplitude of shear velocity variations down to 150 km depth.

10.2. Continental Lithosphere

[111] Pronounced high-velocity continental roots are present beneath some Precambrian tectonic units (western Yangtze Craton, Ordos Plateau, Songliao Basin, and northern Australia) but absent between others (eastern Yangtze and Sino-Korean Cratons, Khorat Basin). The absence of the roots can be explained by extensive deformation of ancient continental lithosphere and its gradual replacement with asthenospheric material. The depth extent of the high-velocity anomalies (where present) varies on a scale of a few hundred kilometers. The roots can extend laterally beyond the present boundaries of the overlying Archean-Proterozoic crust by as much as 500 km. At 120–150 km, S velocity within the ancient continental lithosphere reaches 4.8 km/s; this can be accounted for by thermal and compositional effects.

10.3. Intraplate Volcanism and the Hainan Plume

[112] The sites of Cenozoic intraplate volcanism in the eastern China and Indochina are located above low-velocity

anomalies extending down to about 350 km. Beneath the Hainan Island area in south China a continuous slow anomaly reaches the lower transition zone, the bottom of our model. According to recent whole mantle tomography, low velocities are also present in the lower mantle beneath the region. The hot spot-type volcanism occurring in this location may be caused by the deep-mantle Hainan plume.

10.4. Sea of Japan

[113] A low-velocity mantle domain underlies the south central Sea of Japan, surrounded on the surface by sites of abundant intraplate volcanism. At 120–160 km S velocity is as low as 4.1 km/s, probably indicating partial melting. The subducting Pacific slab separates this zone of low velocities from a deep plume-like slow anomaly imaged by Zhao *et al.* [2000]. A gap in the deep seismicity is present near 40°N and may be a result of the plume-slab interaction.

10.5. Shear Velocities in Subducting Slabs

[114] The S velocity structure of subducting slabs can be resolved down to 660 km depth using multimode surface waves. The locations of the observed high- S velocity anomalies are consistent with deep seismicity data and the results of the high-resolution P wave imaging.

10.6. Long-Lived High-Velocity Anomalies in the Transition Zone

[115] There exist long-term anomalous high-velocity domains in the TZ, such as the one that we observe near the northern boundary of the Yangtze Craton. The anomaly might be due to exceptionally long (>50 m.y.) stagnation in the TZ of subducted oceanic lithospheric material. Our preferred explanation, however, is the stagnation of subducted continental lithosphere, less dense than oceanic lithosphere and unable to penetrate the 660-km discontinuity.

[116] **Acknowledgments.** We are grateful to IRIS-DMC, E. R. Engdahl, R. van der Hilst, R. Buland, and the Harvard seismology group for making available to us the seismograms and the catalogues of the earthquake hypocenters and the CMT solutions used in this study. We thank Suzan van der Lee, who wrote the linear inversion program package that we used, and Jason Morgan, Bill Griffin, Frederik Simons, and Jun Korenaga for discussions on the origins of magmatism in south China, properties of the SE Asian and Australian lithosphere, and the hypothetical plume-slab interaction beneath Japan. Constructive reviews by Saskia Goes, Stephan Sobolev, Federica Marone, and three anonymous referees are appreciated. Figures were prepared with GMT [Wessel and Smith, 1995]. This research was supported through NSF grants EAR-9814570 and EAR-9526372.

References

- Bénard, F., C. Muller, J. Letouzey, C. Rangin, and S. Tahir, Evidence of multiphase deformation in the Rajang-Crocker Range (northern Borneo) from Landsat imagery interpretation: Geodynamic implications, *Tectonophysics*, **183**, 321–339, 1990.
- Bijwaard, H., W. Spakman, and E. R. Engdahl, Closing the gap between regional and global travel time tomography, *J. Geophys. Res.*, **103**, 30,055–30,078, 1998.
- Braias, A., P. Patriat, and P. Tapponnier, Updated interpretation of magnetic anomalies and seafloor spreading stages in the South China Sea: Implications for the Tertiary tectonics of Southeast Asia, *J. Geophys. Res.*, **98**, 6299–6328, 1993.
- Burke, K., and J. T. Wilson, Hot spots on the Earth's surface, *Sci. Am.*, **235**(2), 46–57, 1976.
- Cara, M., and J. J. Lévesque, Waveform inversion using secondary observables, *Geophys. Res. Lett.*, **14**, 1046–1049, 1987.
- Castle, J. C., K. C. Creager, J. P. Winchester, and R. D. van der Hilst, Shear wave speeds at the base of the mantle, *J. Geophys. Res.*, **98**, 21,543–21,557, 2000.
- Chamot-Rooke, N., V. Renard, and X. Le Pichon, Magnetic anomalies in the Shikoku Basin: A new interpretation, *Earth Planet. Sci. Lett.*, **83**, 214–228, 1987.
- Curtis, A., and J. H. Woodhouse, Crust and upper mantle shear velocity structure beneath the Tibetan Plateau and surrounding regions from interevent surface wave phase velocity inversion, *J. Geophys. Res.*, **102**, 11,789–11,813, 1997.
- Curtis, A., J. Trampert, R. Snieder, and B. Dost, Eurasian fundamental mode surface wave velocities and their relationship with tectonic structures, *J. Geophys. Res.*, **103**, 26,919–26,947, 1998.
- Das, T., and G. Nolet, Crustal thickness estimation using high frequency Rayleigh waves, *Geophys. Res. Lett.*, **22**, 539–542, 1995.
- Debayle, E., SV -wave azimuthal anisotropy in the Australian upper mantle: Preliminary results from automated Rayleigh waveform inversion, *Geophys. J. Int.*, **137**, 747–754, 1999.
- Dziewonski, A. M., and D. L. Anderson, Preliminary reference Earth model, *Phys. Earth Planet. Inter.*, **25**, 297–356, 1981.
- Dziewonski, A. M., A. L. Hales, and E. R. Lapwood, Parametrically simple Earth models consistent with geophysical data, *Phys. Earth Planet. Inter.*, **10**, 12–48, 1975.
- Dziewonski, A. M., G. Ekström, and M. P. Salganik, Centroid-moment tensor solutions for January–March 1994, *Phys. Earth Planet. Inter.*, **86**, 253–261, 1994.
- Ekström, G., Mapping the lithosphere and asthenosphere with surface waves: Lateral structure and anisotropy, in *The History and Dynamics of Global Plate Motions*, *Geophys. Monogr. Ser.*, vol. 121, edited by M. A. Richards, R. G. Gordon, and R. D. van der Hilst, pp. 277–288, AGU, Washington, D. C., 2000.
- Ekström, G., and A. M. Dziewonski, The unique anisotropy of the Pacific upper mantle, *Nature*, **394**, 168–172, 1998.
- Engdahl, E. R., R. van der Hilst, and R. Buland, Global teleseismic earthquake relocation with improved travel times and procedures for depth determination, *Bull. Seismol. Soc. Am.*, **88**, 722–743, 1998.
- Flower, M., K. Tamaki, and N. Hoang, Mantle extrusion: A model for dispersed volcanism and DUPAL-like asthenosphere in East Asia and the western Pacific, in *Mantle Dynamics and Plate Interactions in East Asia*, *Geodyn. Ser.*, vol. 27, edited by M. F. J. Flower *et al.*, pp. 67–88, AGU, Washington, D. C., 1998.
- Frederiksen, A. W., M. G. Bostock, and J. F. Cassidy, S-wave velocity structure of the Canadian upper mantle, *Phys. Earth Planet. Inter.*, **124**, 175–191, 2001.
- Fukao, Y., M. Obayashi, H. Inoue, and M. Nishii, Subducting slabs stagnant in the mantle transition zone, *J. Geophys. Res.*, **97**, 4809–4822, 1992.
- Furumura, M., B. L. N. Kennett, and T. Furumura, Seismic wavefield calculation for laterally heterogeneous earth models, II, The influence of upper mantle heterogeneity, *Geophys. J. Int.*, **139**, 623–644, 1999.
- Gaherty, J. B., T. H. Jordan, and L. S. Gee, Seismic structure of the upper mantle in a central Pacific corridor, *J. Geophys. Res.*, **101**, 22,291–22,309, 1996.
- Gee, L. S., and T. H. Jordan, Generalized seismological data functionals, *Geophys. J. Int.*, **111**, 363–390, 1992.
- Goes, S., R. Govers, and P. Vacher, Shallow mantle temperatures under Europe from P and S wave tomography, *J. Geophys. Res.*, **105**, 11,153–11,169, 2000.
- Griffin, W. L., S. Y. O'Reilly, C. G. Ryan, O. Gaul, and D. A. Ionov, Secular variation in the composition of subcontinental lithospheric mantle: Geophysical and geodynamic implications, in *Structure and Evolution of the Australian Continent*, *Geodyn. Ser.*, vol. 26, edited by M. F. J. Flower *et al.*, pp. 1–26, AGU, Washington, D. C., 1998a.
- Griffin, W. L., A. Zhang, S. Y. O'Reilly, and C. G. Ryan, Phanerozoic evolution of the lithosphere beneath the Sino-Korean craton, in *Mantle Dynamics and Plate Interactions in East Asia*, *Geodyn. Ser.*, vol. 27, edited by M. F. J. Flower *et al.*, pp. 107–126, AGU, Washington, D. C., 1998b.
- Gudmundsson, Ó., and M. Sambridge, A regionalized upper mantle (RUM) seismic model, *J. Geophys. Res.*, **103**, 7121–7136, 1998.
- Hall, R., Reconstructing Cenozoic SE Asia, in *Tectonic Evolution of Southeast Asia*, edited by R. Hall and D. Blundell, *Geol. Soc. Spec. Publ.*, **106**, 153–184, 1996.
- Helffrich, G. R., How good are routinely determined focal mechanisms? Empirical statistics based on a comparison of Harvard, USGS and ERI moment tensors, *Geophys. J. Int.*, **131**, 741–750, 1997.
- Hirth, G., and D. L. Kohlstedt, Water in the oceanic upper mantle: Implications for rheology, melt extraction and the evolution of the lithosphere, *Earth Planet. Sci. Lett.*, **144**, 93–108, 1996.
- Iwamori, H., Transportation of H₂O and melting in subduction zones, *Earth Planet. Sci. Lett.*, **160**, 65–80, 1998.
- Jolivet, L., H. Shibuya, and M. Fournier, Paleomagnetic rotations and the Japan Sea opening, in *Active Margins and Marginal Basins of the West-*

- tern Pacific, *Geophys. Monogr. Ser.*, vol. 88, pp. 355–369, AGU, Washington, D. C., 1995.
- Jordan, T. H., The continental tectosphere, *Rev. Geophys.*, 13, 1–12, 1975.
- Jordan, T. H., Structure and formation of the continental tectosphere, *J. Petrol.*, 11–37, Special Lithosphere Issue, 1988.
- Káráson, H., and R. D. van der Hilst, Constraints on Mantle Convection from seismic tomography, in *The History and Dynamics of Global Plate Motions*, edited by M. A. Richards, R. G. Gordon, and R. D. van der Hilst, *Geophys. Monogr. Ser.*, vol. 121, pp. 277–288, AGU, Washington, D. C., 2000.
- Karato, S., Importance of anelasticity in the interpretation of seismic tomography, *Geophys. Res. Lett.*, 20, 1623–1626, 1993.
- Kato, M., and T. H. Jordan, Seismic structure of the upper mantle beneath the western Philippine Sea, *Phys. Earth Planet. Inter.*, 110, 263–283, 1999.
- Kennett, B. L. N., and G. Nolet, The interaction of the *S*-wavefield with upper mantle heterogeneity, *Geophys. J. Int.*, 101, 751–762, 1990.
- Kennett, B. L. N., E. R. Engdahl, and R. Buland, Constraints on seismic velocities in the Earth from traveltimes, *Geophys. J. Int.*, 122, 108–124, 1995.
- Lallemant, S. E., M. Popoff, J.-P. Cadet, A.-G. Bader, M. Pubellier, C. Rangin, and B. Defontaine, Genetic relations between the central and southern Philippine Trench and the Sangihe Trench, *J. Geophys. Res.*, 103, 933–950, 1998.
- Lebedev, S., The upper mantle beneath the western Pacific and Southeast Asia, Ph.D. thesis, Princeton Univ., Princeton, N. J., 2000.
- Lebedev, S., and G. Nolet, Sensitivity of multimode surface waves and the scale of heterogeneity in the western Pacific upper mantle, *Eos Trans. AGU*, 79(17), Spring Meet. Suppl., S206, 1998.
- Lebedev, S., G. Nolet, and R. D. van der Hilst, The upper mantle beneath the Philippine Sea region from waveform inversions, *Geophys. Res. Lett.*, 25, 1851–1854, 1997.
- Lee, T.-Y., and L. A. Lawver, Cenozoic plate reconstruction of Southeast Asia, *Tectonophysics*, 251, 85–138, 1995.
- Li, S., and W. D. Mooney, Crustal structure of China from deep seismic sounding profiles, *Tectonophysics*, 288, 105–113, 1998.
- Li, Z. X., Tectonic history of the major East Asian lithospheric blocks since the mid-Proterozoic—A synthesis, in *Mantle Dynamics and Plate Interactions in East Asia*, *Geodyn. Ser.*, vol. 27, edited by M. F. J. Flower et al., pp. 221–243, AGU, Washington, D. C., 1998.
- Liou, J. G., R. Y. Zhang, X. M. Wang, E. A. Eide, W. G. Ernst, and S. Maruyama, Metamorphism and tectonics of high-*P* and ultrahigh-*P* belts in the Dabie-Sulu region, eastern central China, in *Tectonic Development of Asia*, Rubey vol. VIII, edited by M. T. Harrison and A. Yin, pp. 300–344, Cambridge Univ. Press, New York, 1996.
- Liou, J. G., B. R. Hacker, and R. Y. Zhang, Into the forbidden zone, *Science*, 287, 1215–1216, 2000.
- Lithgow-Bertelloni, C., and M. Richards, The dynamics of Cenozoic and Mesozoic plate motions, *Rev. Geophys.*, 36, 27–78, 1998.
- Liu, H.-P., D. L. Anderson, and H. Kanamori, Velocity dispersion due to anelasticity; implications for seismology and mantle composition, *Geophys. J. R. Astron. Soc.*, 47, 41–58, 1976.
- Marquering, H., G. Nolet, and F. A. Dahlen, Three-dimensional waveform sensitivity kernels, *Geophys. J. Int.*, 132, 521–534, 1998.
- McKenzie, D., and M. J. Bickle, The volume and composition of melt generated by extension of the lithosphere, *J. Petrol.*, 29, 625–679, 1988.
- Meier, T., and P. G. Malischewsky, Approximation of surface wave mode conversion at a passive continental margin by a mode-matching technique, *Geophys. J. Int.*, 141, 12–24, 2000.
- Meier, T., S. Lebedev, G. Nolet, and F. A. Dahlen, Diffraction tomography using multimode surface waves, *J. Geophys. Res.*, 102, 8255–8267, 1997.
- Menzies, M., and Y. Xu, Geodynamics of the North China Craton, in *Mantle Dynamics and Plate Interactions in East Asia*, *Geodyn. Ser.*, vol. 27, edited by M. F. J. Flower et al., pp. 155–165, AGU, Washington, D. C., 1998.
- Metcalf, I., Pre-Cretaceous evolution of SE Asian terranes, in *Tectonic Evolution of Southeast Asia*, edited by R. Hall and D. Blundell, *Geol. Soc. Spec. Publ.*, 106, 153–184, 1996.
- Molnar, P., and P. Tapponnier, Cenozoic tectonics of Asia: Effects of a continental collision, *Science*, 189, 419–426, 1975.
- Montelli, R., J. Virieux, G. Nolet, A. Lomax, and A. Zollo, Three dimensional linearized seismic tomography of Mt. Vesuvius with irregular model parameterizations, *Eos Trans. AGU*, 81(47), Fall Meet. Suppl., F902, 2000.
- Mooney, W. D., G. Laske, and T. G. Masters, CRUST 5.1: A global crustal model at 5° × 5°, *J. Geophys. Res.*, 103, 727–747, 1998.
- Mrozowski, C. L., and D. E. Hayes, The evolution of the Parece Vela basin, eastern Philippine Sea, *Earth Planet. Sci. Lett.*, 46, 49–67, 1979.
- Nakamura, E., I. H. Campbell, M. T. McCulloch, and S.-S. Sun, Chemical geodynamics in a back arc region around the Sea of Japan: Implications for the genesis of alkaline basalts in Japan, Korea, and China, *J. Geophys. Res.*, 94, 4634–4654, 1989.
- Nakamura, Y., and T. Shibutani, Three-dimensional shear velocity structure in the upper mantle beneath the Philippine Sea region, *Earth Planets Space*, 50, 939–952, 1998.
- Nolet, G., Partitioned waveform inversion and two-dimensional structure under the Network of Autonomously Recording Seismographs, *J. Geophys. Res.*, 95, 8499–8512, 1990.
- Nolet, G., and A. Zielhuis, Low *S* velocities under the Tornquist-Teisseyre zone: Evidence for water injection into the transition zone by subduction, *J. Geophys. Res.*, 99, 15,813–15,820, 1994.
- Nolet, G., R. Montelli, and J. Virieux, Explicit, approximate expressions for the resolution and a posteriori covariance of massive tomographic systems, *Geophys. J. Int.*, 138, 36–44, 1999.
- Oda, H., and N. Senna, Regional variation in surface wave group velocities in the Philippine Sea, *Tectonophysics*, 233, 265–277, 1994.
- Osozawa, S., Major transform duplexing along the eastern margin of Cretaceous Eurasia, in *Mantle Dynamics and Plate Interactions in East Asia*, *Geodyn. Ser.*, vol. 27, edited by M. F. J. Flower et al., pp. 245–257, AGU, Washington, D. C., 1998.
- Packham, G., Cenozoic SE Asia: reconstructing its aggregation and reorganization, in *Tectonic Evolution of Southeast Asia*, edited by R. Hall and D. Blundell, *Geol. Soc. Spec. Publ.*, 106, 153–184, 1996.
- Ritzwoller, M. H., and A. L. Levshin, Eurasian surface wave tomography: Group velocities, *J. Geophys. Res.*, 103, 4839–4878, 1998.
- Savage, M., Seismic anisotropy and mantle deformation: What have we learned from shear wave splitting?, *Rev. Geophys.*, 37, 65–106, 1999.
- Schmeling, H., Numerical models of the influence of partial melt on elastic, anelastic, and electric properties of rocks, part 1, Elasticity and anelasticity, *Phys. Earth Planet. Inter.*, 41, 34–57, 1985.
- Seekins, L. C., and T. Teng, Lateral variations in the structure of the Philippine Sea plate, *J. Geophys. Res.*, 82, 317–324, 1977.
- Seno, T., and S. Maruyama, Paleogeographic reconstruction and origin of the Philippine Sea, *Tectonophysics*, 102, 53–84, 1984.
- Simons, F. J., A. Zielhuis, and R. D. van der Hilst, The deep structure of the Australian continent from surface-wave tomography, *Lithos*, 48, 17–43, 1999.
- Simons, F. J., R. D. van der Hilst, J.-P. Montagner, and A. Zielhuis, Multimode Rayleigh wave inversion for heterogeneity and azimuthal anisotropy of the Australian upper mantle, *Geophys. J. Int.*, 151, in press, 2002.
- Smith, A. D., The geodynamic significance of the DUPAL anomaly in Asia, in *Mantle Dynamics and Plate Interactions in East Asia*, *Geodyn. Ser.*, vol. 27, edited by M. F. J. Flower et al., pp. 89–105, AGU, Washington, D. C., 1998.
- Sobolev, S. V., H. Zeyen, G. Stoll, F. Werling, R. Altherr, and K. Fuchs, Upper mantle temperatures from teleseismic tomography of French Massif Central including effects of composition, mineral reactions, anharmonicity, anelasticity and partial melt, *Earth Planet. Sci. Lett.*, 139, 147–163, 1996.
- Su, W.-J., R. L. Woodward, and A. M. Dziewonski, Degree 12 model of shear velocity heterogeneity in the mantle, *J. Geophys. Res.*, 99, 6945–6980, 1994.
- Tajima, F., and S. P. Grand, Variation of transition zone high-velocity anomalies and depression of 660-km discontinuity associated with subduction zones from the southern Kurile to Izu-Bonin and Ryukyu, *J. Geophys. Res.*, 103, 15,015–15,036, 1998.
- Tu, K., M. F. J. Flower, R. W. Carlson, M. Zhang, and G. Xie, Sr, Nd, and Pb isotopic compositions of Hainan basalts (south China): Implications for a subcontinental lithosphere Dupal source, *Geology*, 19, 567–569, 1991.
- Van der Hilst, R. D., and T. Seno, Effects of relative plate motion on the deep structure and penetration depth of slabs below the Izu-Bonin and Mariana island arcs, *Earth Planet. Sci. Lett.*, 120, 395–407, 1993.
- Van der Hilst, R. D., E. R. Engdahl, W. Spakman, and G. Nolet, Tomographic imaging of subducted lithosphere below northwest Pacific island arcs, *Nature*, 353, 37–43, 1991.
- Van der Lee, S., Observations and origin of Rayleigh-wave amplitude anomalies, *Geophys. J. Int.*, 135, 691–699, 1998.
- Van der Lee, S., and G. Nolet, Seismic image of the subducted trailing fragments of the Farallon Plate, *Nature*, 386, 266–269, 1997a.
- Van der Lee, S., and G. Nolet, Upper mantle *S* velocity structure of North America, *J. Geophys. Res.*, 102, 22,815–22,838, 1997b.
- Van Heijst, H. J., and J. H. Woodhouse, Measuring surface-wave overtone phase velocities using a mode branch stripping technique, *Geophys. J. Int.*, 131, 209–230, 1997.
- Van Heijst, H. J., J. Ritsema, and J. H. Woodhouse, Global *P* and *S* velocity structure derived from normal mode splitting, surface wave dispersion, and body wave travel time data, *EOS Trans. AGU*, 80(17), Spring Meet. Suppl., S221, 1999.
- Walsh, J. B., New analysis of attenuation in partially melted rock, *J. Geophys. Res.*, 74, 4333–4337, 1969.

- Wang, Z., and F. A. Dahlen, Validity of surface-wave ray theory on a laterally heterogeneous earth, *Geophys. J. Int.*, 123, 757–773, 1995.
- Weissel, J. K., and R. N. Anderson, Is there a Caroline plate?, *Earth Planet. Sci. Lett.*, 41, 143–158, 1978.
- Wessel, P., and W. H. F. Smith, New version of the Generic Mapping Tools released, *Eos Trans. AGU*, 76, 329, 1995.
- Widiyantoro, S., and R. van der Hilst, Mantle structure beneath Indonesia inferred from high-resolution tomographic imaging, *Geophys. J. Int.*, 130, 167–182, 1997.
- Yuan, X., Velocity structure of the Qinling lithosphere and the mushroom cloud model, *Sci. China, Ser. D*, 39, 235–244, 1996.
- Zhang, M., X.-H. Zhou, and J.-B. Zhang, Nature of the lithospheric mantle beneath NE China: Evidence from potassic volcanic rocks and mantle xenoliths, in *Mantle Dynamics and Plate Interactions in East Asia, Geodyn. Ser.*, vol. 27, edited by M. F. J. Flower et al., pp. 197–219, AGU, Washington, D. C., 1998.
- Zhang, Z. M., J. G. Liou, and R. G. Coleman, An outline of the plate tectonics of China, *Geol. Soc. Am. Bull.*, 95, 295–312, 1984.
- Zhao, D., Y. Fukao, and T. Seno, A plume-like slow anomaly under the subducting Pacific slab beneath central Japan, *Eos Trans. AGU*, 81(22), West. Pac. Geophys. Meet. Suppl., W137, 2000.
-
- S. Lebedev, MIT, EAPS, Room 54-512, Cambridge, MA 02139, USA. (sergei@quake.mit.edu)
- G. Nolet, Princeton University, Department of Geosciences, Princeton, NJ 08544, USA. (nolet@princeton.edu)